

INFRARED PROPERTIES OF STAR-FORMING DWARF GALAXIES. I. DWARF IRREGULAR GALAXIES IN THE LOCAL VOLUME¹

OVIDIU VADUVESCU AND MARSHALL L. MCCALL

Department of Physics and Astronomy, York University, 4700 Keele Street, Toronto, ON M3J 1P3, Canada;
ovidiu@yorku.ca, mccall@yorku.ca

MICHAEL G. RICHER

Observatorio Astronómico Nacional, Instituto de Astronomía, UNAM, P.O. Box 439027, San Diego, CA 92143-9027;
richer@astrosen.unam.mx

AND

ROBIN L. FINGERHUT

Department of Physics and Astronomy, York University, 4700 Keele Street, Toronto, ON M3J 1P3, Canada; rfinger@yorku.ca

Received 2004 December 14; accepted 2005 June 27

ABSTRACT

A sample of 34 dwarf irregular galaxies (dIs) in the Local Volume, most nearer than 5 Mpc, has been imaged in the near-infrared (NIR) in J and K_s at the Canada-France-Hawaii Telescope (CFHT) in Hawaii and the Observatorio Astronómico Nacional in the Sierra San Pedro Mártir, in Mexico. Absolute magnitudes in K_s range from -14 to -18 . In the CFHT images, stars brighter than $M_{K_s} \sim -7.5$ were resolved. We show that the resolved component comprises more than 50% of the light from star formation bursts within the last 3 Gyr. In most cases, the resolved population down to $M_{K_s} = -7.5$ represents less than 5% of the total NIR flux in K_s , with fractions in J being 1.5–2 times larger. Thus, the NIR light of dIs can be considered to be predominantly contributed by stars older than about 4 Gyr. Although exponential at large radii, surface brightness profiles for the unresolved component flatten in the centers. They can be fitted across the whole range of radii with a hyperbolic secant (sech) defined as a function of two parameters: the central surface brightness and the scale length of the exponential. With respect to this model, only two galaxies (NGC 1569 and NGC 3738) show an excess of flux in the center, both of which are hosting starbursts. Isophotal, total, and fitted sech magnitudes have been calculated for all galaxies for which the unresolved component was detected, along with semimajor axes at $\mu_J = 23$ mag arcsec⁻² and $\mu_{K_s} = 22$ mag arcsec⁻². The scale length and the semimajor axes correlate linearly with absolute isophotal magnitude. The same is true for colors and the central brightness. More luminous dIs tend to be larger, redder, and brighter in the center. The fraction of light contributed by young stars is independent of both luminosity and central surface brightness. The Tully-Fisher relation shows considerable scatter, but residuals are tied to surface brightness. The galaxies appear to lie in a “fundamental plane” defined by the sech absolute magnitude, the sech central surface brightness, and the H I line width. The rms of residuals in M_K is only 0.4 mag, which implies that the plane can be used to evaluate the distances of star-forming dwarfs. Corrections for tilt do not reduce the residuals, so line widths must be governed predominantly by random motions. Color-magnitude diagrams (CMDs) are presented for 29 galaxies in which stars were resolved. Most show a finger centered around $J - K_s = 1$ mag. In some cases, there is a red tail extending to $J - K_s = 2.5$ mag. Most color profiles constructed for the unresolved component show a remarkably constant $J - K_s = 0.8$ – 1.0 mag, matching the color of the finger in the CMDs.

Key words: galaxies: fundamental parameters — galaxies: irregular — galaxies: photometry — galaxies: stellar content

1. INTRODUCTION

Dwarfs are the most numerous galaxies in the universe. Defined as having absolute magnitudes fainter than $M_V \sim -18$ mag (Grebel 2001), dwarf galaxies are organized in four groups based on their optical appearance: dwarf elliptical galaxies (dEs), dwarf spheroidal galaxies, dwarf irregular galaxies (dIs), and blue compact dwarfs (BCDs).

Among dwarfs, dIs and BCDs are considered the building blocks for more massive galaxies in hierarchical merger scenarios. As such, they are important probes for studying matter in its near-primordial state. Despite much work in the last two decades, many questions remain open about dwarf galaxies, the

most important being the evolutionary links between dIs, BCDs, and dEs. Some authors suggest that BCDs and dIs are the same type of galaxy, with BCDs being dIs undergoing bursts of star formation (e.g., Thuan 1985). Others argue that dIs are a fundamentally distinct type from BCDs, with no simple evolutionary links between them (e.g., James 1994; Richer & McCall 1995). Papaderos et al. (1996) review previous arguments on the evolutionary relationships between BCDs, dIs, and dEs without reaching firm conclusions.

Having a low surface brightness ($\mu_B \geq 22$ mag arcsec⁻²), dIs are gas-rich galaxies showing no nucleation and with an irregular optical appearance usually dominated by scattered H II regions, associated with star formation. The proportion of metals in dIs is very low, with metallicities (Z) ranging between 1/40 and 1/3 Z_\odot (Kunth & Östlin 2000). Skillman et al. (1989) confirmed a strong correlation between absolute magnitude and metallicity for local dIs, in the sense that the least luminous are the most metal-poor.

¹ Based on observations obtained at the Canada-France-Hawaii Telescope, which is operated by the National Research Council of Canada, the Centre National de la Recherche Scientifique de France, and the University of Hawaii; also based on data acquired at OAN-SPM in Mexico.

The existence of a relation between metallicity and luminosity constitutes a manifestation of something deeper that needs to be understood in order to address the chemical evolution of dwarf galaxies (Kunth & Östlin 2000).

According to Kunth & Östlin (2000), the origin of the concepts of “compact galaxies” and “blue compact galaxies” (BCGs) is due to Zwicky (1965). Those BCGs that are less luminous than $M_B \approx -17$ are commonly referred to as “blue compact dwarfs.” BCDs include gas, stars, and usually starburst regions, all of which are centrally concentrated. Due to their pronounced compact starbursts, BCDs have higher surface brightnesses ($\mu_B \leq 22$ mag arcsec⁻²). Like dIs, BCDs are also metal-poor, with Z as low as $1/50 Z_\odot$, showing a trend of redder colors toward higher metallicities (Thuan 1983).

Most of our knowledge about dwarfs comes from members of the Local Volume, i.e., our neighborhood within about 10 Mpc (Karachentsev et al. 2004), whose stellar content can now be studied in detail using large ground-based facilities or the *Hubble Space Telescope*. Additional information comes from studies of the global properties of dwarfs in clusters.

The utility of light as a gauge of galaxy mass depends on the wavelength of observation. In star-forming galaxies such as dIs and BCDs, the young population shines brightly in the visible, overwhelming the light from the old stellar component, which constitutes the bulk of the mass. This problem can be minimized in the near-infrared (NIR), where the intermediate-age and old populations become more visible. Furthermore, light in the NIR is much less attenuated by extinction than light in the visible. More data in the NIR have become available with the advancement of NIR technology in the last decade. NIR photometry is now available from deep studies of selected objects, as well as from shallower but more homogeneous surveys such as the Two Micron All Sky Survey (2MASS) or DENIS. Despite these efforts, well-defined stellar populations such as the asymptotic giant branch (AGB) and the red giant branch (RGB) have been identified in the NIR in only a few close dIs, such as IC 10 (Borissova et al. 2000b), IC 1613 (Borissova et al. 2000a), NGC 1569 (Aloisi et al. 2001), NGC 4214 (Drozdovsky et al. 2002), NGC 1705 (Tosi et al. 2001), the Magellanic Clouds (Nikolaev & Weinberg 2000; Cioni & Habing 2003), and NGC 6822 (Cioni & Habing 2005). Thus, more work needs to be done in this direction.

In § 2 we present the selection criteria for our observing sample. In § 3 we describe our observations. The image reduction method is presented in § 4, followed by the photometric calibration in § 5. In § 6 the stellar photometry is addressed, and the catalogs of selected stars from which color-magnitude diagrams (CMDs) were constructed are described. Surface photometry is presented and analyzed in § 7. In § 8 the NIR properties of the dIs are discussed, based on correlations between their sizes, central surface brightnesses, unresolved fluxes, and the ratios of the flux from the resolved light to the total light. Distances taken from the literature are homogenized to a common distance scale, used throughout the paper, and presented in the Appendix. Conclusions are presented in § 9.

2. THE SAMPLE

In previous studies of dwarf galaxies in the field (Lee et al. 2003b; Richer & McCall 1995), samples were defined based on two criteria:

1. Detection of the [O III] $\lambda 4363$ emission line for the determination of oxygen abundances.
2. A reliable distance (i.e., determined from stellar constituents, such as Cepheids and the tip of the RGB [TRGB]).

The observing facilities to which we had access imposed two additional criteria on our sample:

3. An apparent size smaller than $\sim 3'$, possible to image by both facilities used for this work.
4. Target visibility from each facility during the observing time granted.

We identified 34 dwarf galaxies that satisfied these conditions. They are listed in Table 1.

3. OBSERVATIONS

Between 2001 and 2004, we had six observing runs (27 nights in total) during which we observed 34 field dwarfs in the NIR. Of these, a total of about 12 nights were used to observe the field dIs. The remaining 15 nights were dedicated to BCDs in the Virgo Cluster. All allocated observing time was bright (the Moon was within 5 days of full). Our observations of the field dIs are presented in this paper. The observations of the Virgo BCDs will be included in a future paper.

We obtained our observations using the 3.6 m Canada-France-Hawaii Telescope (CFHT) located atop Mauna Kea, Hawaii, and the 2.1 m telescope of the Observatorio Astronómico Nacional in the Sierra San Pedro Mártir (OAN-SPM) in Baja California, Mexico. Due to cloudiness (especially in Mexico), the observing efficiency was about half of the allocated time. Consequently, data for field dIs were acquired on about six nights in total (three at CFHT and three at OAN-SPM). A log of our observations of the 34 field dIs is presented in Table 1.

Observing faint extended sources in the NIR is difficult because the sky is very bright in the NIR, with an average surface brightness of $\mu_K \sim 13$ mag arcsec⁻² for a dark site such as Mauna Kea.² Furthermore, the surface brightness of the isophote defining D_{25} in the B band corresponds to 21–23 mag arcsec⁻² in K (e.g., Fioc & Rocca-Volmerange 1999). In the K band, this faint surface brightness makes galaxies 8–10 mag fainter than the sky! An additional problem is the background due to the atmosphere, detector, and thermal radiation, which vary both temporally and spatially. Thus, conservative approaches to observing and reductions were taken to ensure accurate background subtraction, the details of which are given below (see also Vaduvescu & McCall 2004).

3.1. CFHT Observations

On three nights between 2002 February 28 and March 3, we observed 26 field dIs in J and K_s at the 3.6 m f/8 Cassegrain focus of CFHT. We employed the CFHT-IR camera, which is equipped with a HgCdTe array with 1024×1024 pixels. The scale was $0''.211$ pixel⁻¹, yielding a $3'.6 \times 3'.6$ field of view (FOV).

Two other nights between 2004 March 6 and 8 were used to observe three more dIs as part of another project (R. L. Fingerhut et al. 2005, in preparation). For these three targets, we employed the same instrument described above.

In 2002 conditions were photometric on all three nights, with an average seeing of $0''.5$ in K_s , humidity less than 30%, and a steady temperature of about -2°C ,³ all typical of Mauna Kea when weather is good. The two nights in 2004 were photometric, with the temperature dropping from $+2^\circ\text{C}$ to -4°C and the humidity oscillating between 10% and 30% for most of the run.

² See the online documentation by L. Vanzani & O. R. Hainaut at the European Southern Observatory; <http://www.eso.org/gen-fac/pubs/astclim/lasilla/l-vanzani-poster>.

³ See UKIRT Graphical Weather Server, online at http://www.ukirt.jach.hawaii.edu/weather_server/weather.cgi.

TABLE 1
OBSERVING LOG

Galaxy	Observatory	Date (UT)	Filter	Exposure Time (s)
Cas 1	OAN-SPM	2002 Mar 1	K_s	1800
	OAN-SPM	2003 Mar 15	J	1200
MB 1	CFHT	2002 Mar 2	K_s	600
	CFHT	2002 Mar 2	J	300
Cam A.....	CFHT	2002 Mar 3	K_s	600
	CFHT	2002 Mar 3	J	300
NGC 1569.....	CFHT	2002 Mar 1	K_s	600
	CFHT	2002 Mar 1	J	300
	OAN-SPM	2002 Feb 28	K_s	2160
	OAN-SPM	2002 Feb 28	J	1020
UGCA 92.....	CFHT	2002 Mar 2	K_s	600
	CFHT	2002 Mar 2	J	300
Orion dwarf.....	CFHT	2002 Mar 3	K_s	600
	CFHT	2002 Mar 3	J	300
DDO 47.....	CFHT	2002 Mar 2	K_s	600
	CFHT	2002 Mar 2	J	300
UGC 4115.....	CFHT	2002 Mar 2	K_s	600
	CFHT	2002 Mar 2	J	300
DDO 53.....	CFHT	2002 Mar 1	K_s	600
	CFHT	2002 Mar 1	J	300
	OAN-SPM	2001 Mar 2	K_s	2760
UGC 4483.....	CFHT	2004 Feb 24	K_s	525
	CFHT	2004 Feb 24	J	300
	OAN-SPM	2004 Feb 12, 17	K_s	4320
	OAN-SPM	2004 Feb 12, 16	J	2400
UGC 4998.....	OAN-SPM	2004 Feb 13	K_s	2340
	OAN-SPM	2004 Feb 13	J	1200
Ho I.....	CFHT	2002 Mar 3	K_s	600
	CFHT	2002 Mar 3	J	300
Leonis A	CFHT	2002 Mar 3	K_s	600
	CFHT	2002 Mar 3	J	300
Sextans B	CFHT	2002 Mar 3	K_s	600
	CFHT	2002 Mar 3	J	300
UGC 5423.....	CFHT	2004 Mar 7	K_s	525
	CFHT	2004 Mar 7	J	300
Sextans A.....	CFHT	2004 Mar 8	K_s	600
	CFHT	2004 Mar 8	J	300
UGC 5692.....	CFHT	2002 Mar 3	K_s	600
	CFHT	2002 Mar 3	J	300
UGC 5848.....	OAN-SPM	2003 Mar 17, 19	K_s	2040
	OAN-SPM	2003 Mar 15	J	1200
UGC 5979.....	OAN-SPM	2004 Feb 15	K_s	1140
	OAN-SPM	2004 Feb 15	J	1200
UGC 6456.....	CFHT	2002 Mar 1	K_s	600
	CFHT	2002 Mar 1	J	300
Mrk 178	CFHT	2002 Mar 2	K_s	600
	CFHT	2002 Mar 2	J	300
NGC 3738.....	CFHT	2002 Mar 1	K_s	600
	CFHT	2002 Mar 1	J	300
NGC 3741.....	CFHT	2002 Mar 3	K_s	600
	CFHT	2002 Mar 3	J	300
NGC 4163.....	CFHT	2002 Mar 3	K_s	600
	CFHT	2002 Mar 3	J	300
NGC 4190.....	CFHT	2002 Mar 3	K_s	600
	CFHT	2002 Mar 3	J	300
Mrk 209	CFHT	2002 Mar 1	K_s	600
	CFHT	2002 Mar 1	J	300
PGC 42275	CFHT	2002 Mar 2	K_s	600
	CFHT	2002 Mar 2	J	300
NGC 4789A.....	CFHT	2002 Mar 1	K_s	600
	CFHT	2002 Mar 1	J	300
GR 8.....	CFHT	2002 Mar 2, 3	K_s	1200
	CFHT	2002 Mar 2, 3	J	600

TABLE 1—Continued

Galaxy	Observatory	Date (UT)	Filter	Exposure Time (s)
DDO 167.....	CFHT	2002 Mar 1	K_s	600
	CFHT	2002 Mar 1	J	300
UGC 8508.....	OAN-SPM	2002 Mar 1	K_s	2520
	OAN-SPM	2002 Mar 1	J	900
NGC 5264.....	CFHT	2002 Mar 2	K_s	600
	CFHT	2002 Mar 2	J	300
Ho IV.....	CFHT	2002 Mar 3	K_s	600
	CFHT	2002 Mar 3	J	300
DDO 187.....	CFHT	2002 Mar 1, 2	K_s	1200
	CFHT	2002 Mar 1, 2	J	600
	OAN-SPM	2001 Mar 3	K_s	2940

One of the main objectives of the present project is to disentangle the young stellar population from the old. We aimed to resolve young stars down to an absolute magnitude $\mu_{K_s} = -7.5$ mag, i.e., AGB stars younger than roughly 8.5 Gyr (Bressan et al. 1994; see their Fig. 25 and Table 2), assuming a metallicity of $Z = 0.001 Z_{\odot}$. Calculated at a distance of 5 Mpc (the limit for most of our targets), this absolute magnitude limit corresponds to an apparent magnitude $K_s = 21$ mag. We also aimed to detect isophotes as faint as $\mu_{K_s} = 23$ mag arcsec $^{-2}$ and $\mu_J = 24$ mag arcsec $^{-2}$, i.e., as faint in the outer parts of the galaxy as $\mu_B = 25$ mag arcsec $^{-2}$. In order to reach these limits, we used total exposure times of 10 minutes in K_s and 5 minutes in J . In 2002 this was obtained by combining individual exposures of 60 s in K_s and 100 s in J . In 2004 we combined exposures of 75 s in K_s and 60 s in J .

Based on a statistical analysis that we performed on a representative data set (800 images taken in K_s and J during three photometric nights using the CFHT-IR camera in 2002), we derived some results regarding the variation of the sky background (Vaduvescu & McCall 2004). At the CFHT, the *background level* (defined as the median signal in any given sky frame) varies from frame to frame by about 0.5% minute $^{-1}$ in K_s and 0.7% minute $^{-1}$ in J , on average. The *background pattern* (defined across the $3'6 \times 3'6$ FOV by the range of count levels in frame differences) varies on average by about 0.2% minute $^{-1}$ in K_s and 0.3% minute $^{-1}$ in J .

In order to detect the outermost regions of the dwarfs, which is where the old population is expected to make the largest contribution to the light, we sampled the sky as often as the target, using the same exposure time for both target and sky. This was done in order to properly account for temporal variations in the NIR background. The spatial signature was removed using a flat field derived for each filter from twilight sky images taken each night or morning.

We employed the following observing sequence:

$$\text{sky-target-sky-target-sky-} \dots \text{-sky-target-sky.} \quad (1)$$

Sky frames were observed in the same region of sky as each galaxy, namely, $4' - 5'$ north or south of the target. To improve the identification of bad pixels and to remove small contaminants, we adopted the classical approach of dithering each new sky frame and each new galaxy frame by $5'' - 10''$ with respect to the previous sky or galaxy frame.

3.2. OAN-SPM Observations

Between 2001 and 2004 we were granted four observing runs for a total of 21 nights at the f/4.5 focus of the 2.1 m telescope at OAN-SPM. In all runs we used the CAMILA NIR camera,

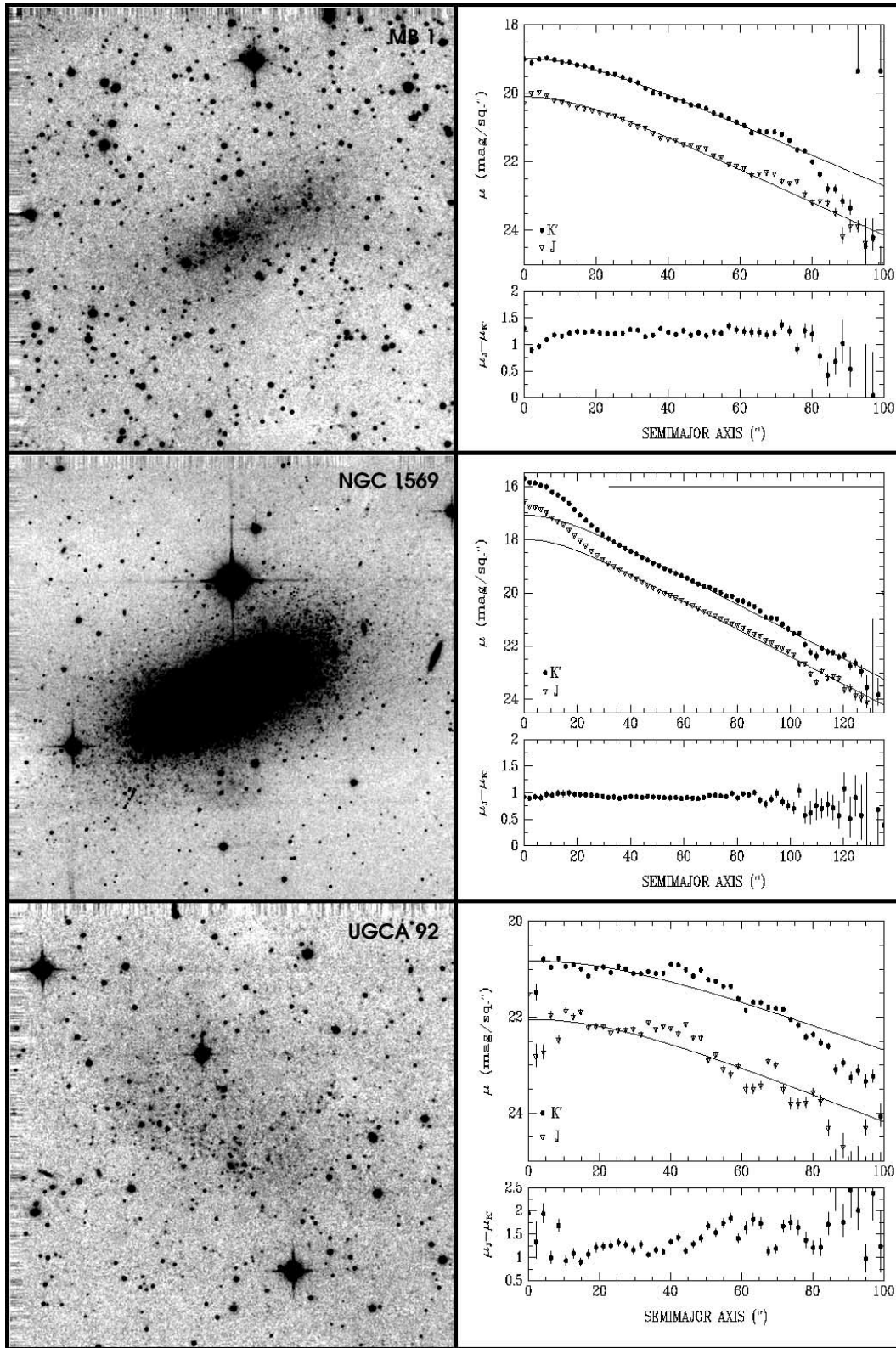


FIG. 1.—Field dwarf galaxies observed at CFHT for which an unresolved component was detected. *Left panels:* K_s images (north is up and east to the left; FOV is $3'.6 \times 3'.6$, binned 4×4). *Right panels:* SBPs in J and K_s (upper plots) and $J - K_s$ color profiles (lower plots).

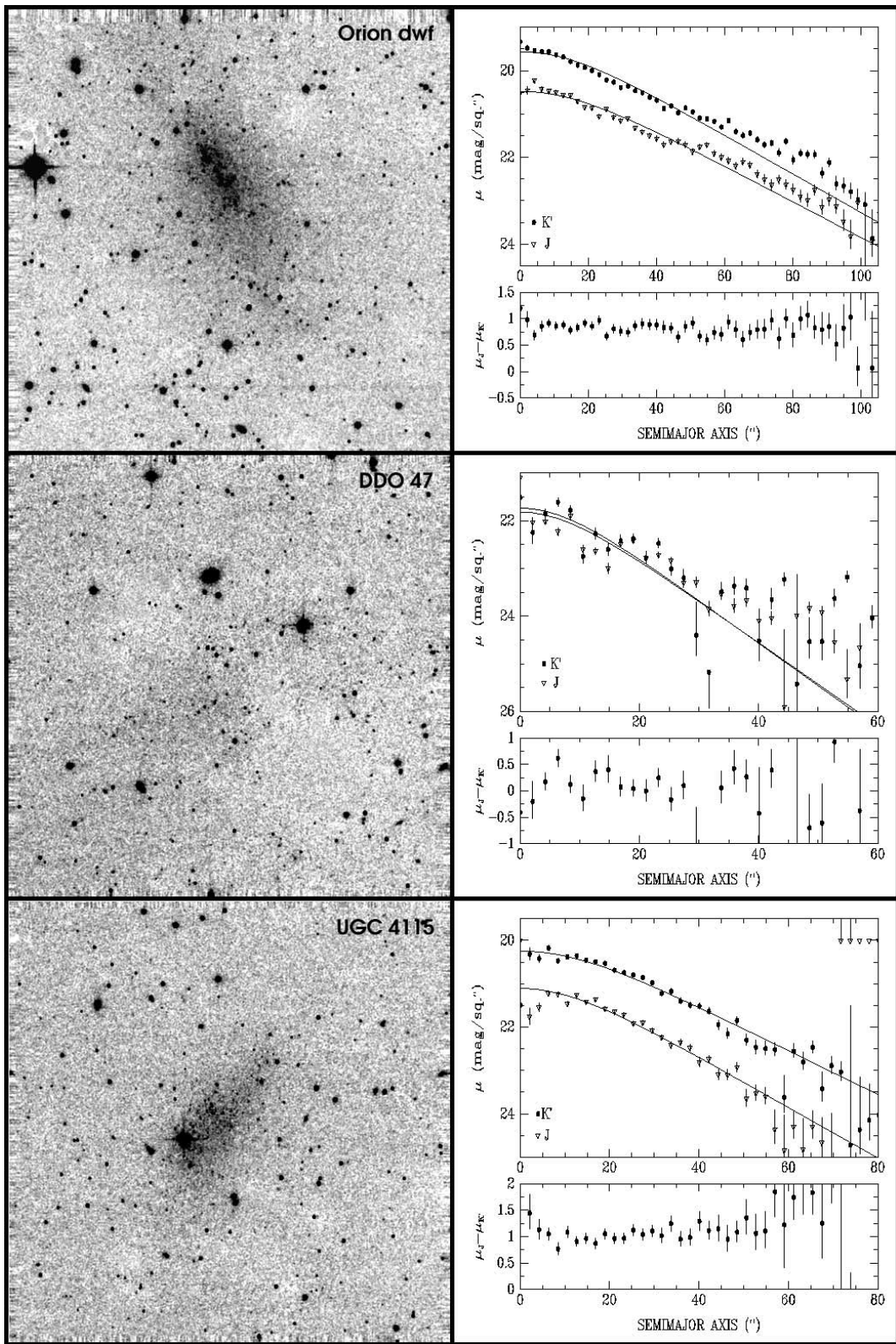


FIG. 1.—Continued

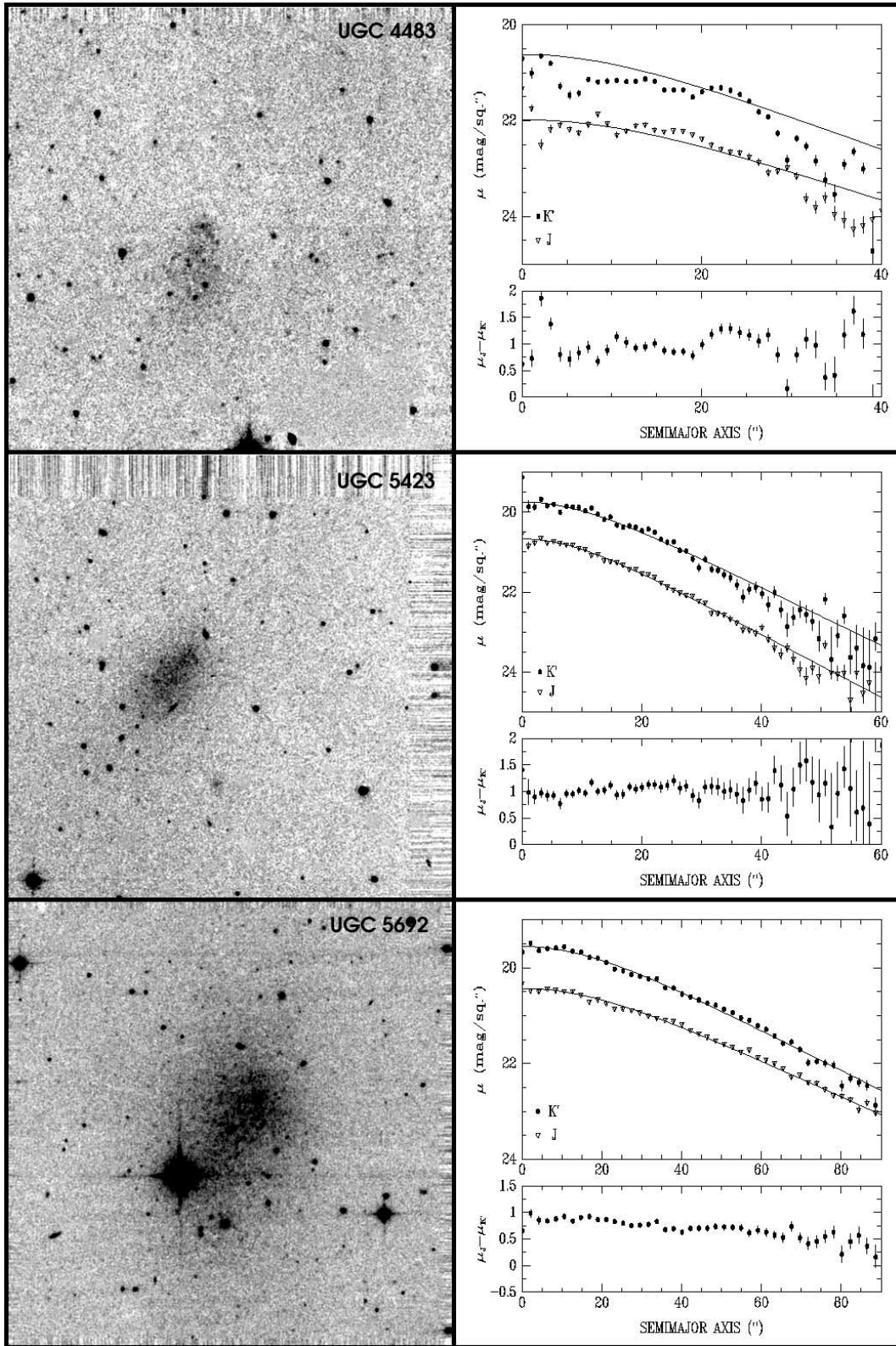


FIG. 1.—Continued

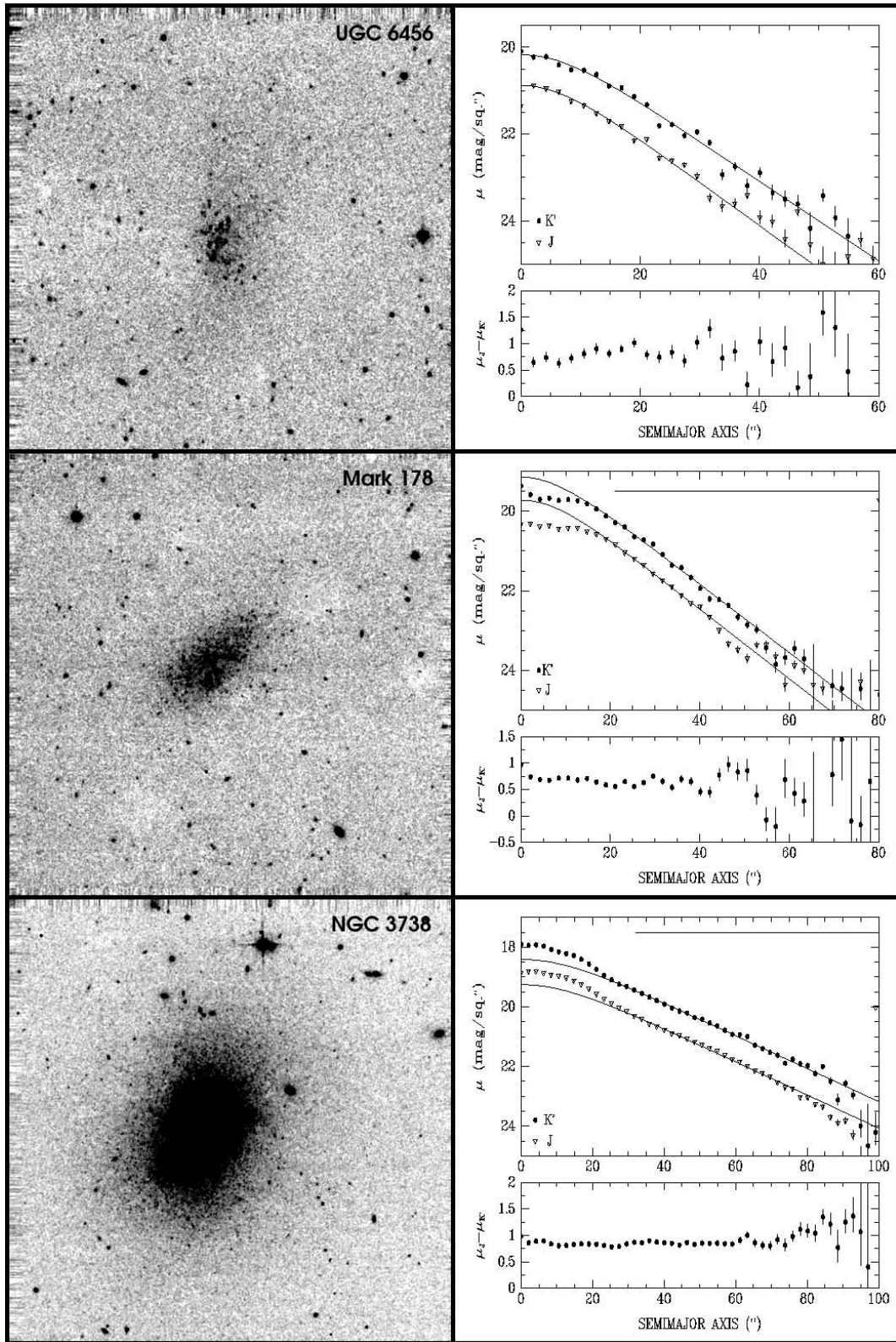


FIG. 1.—Continued

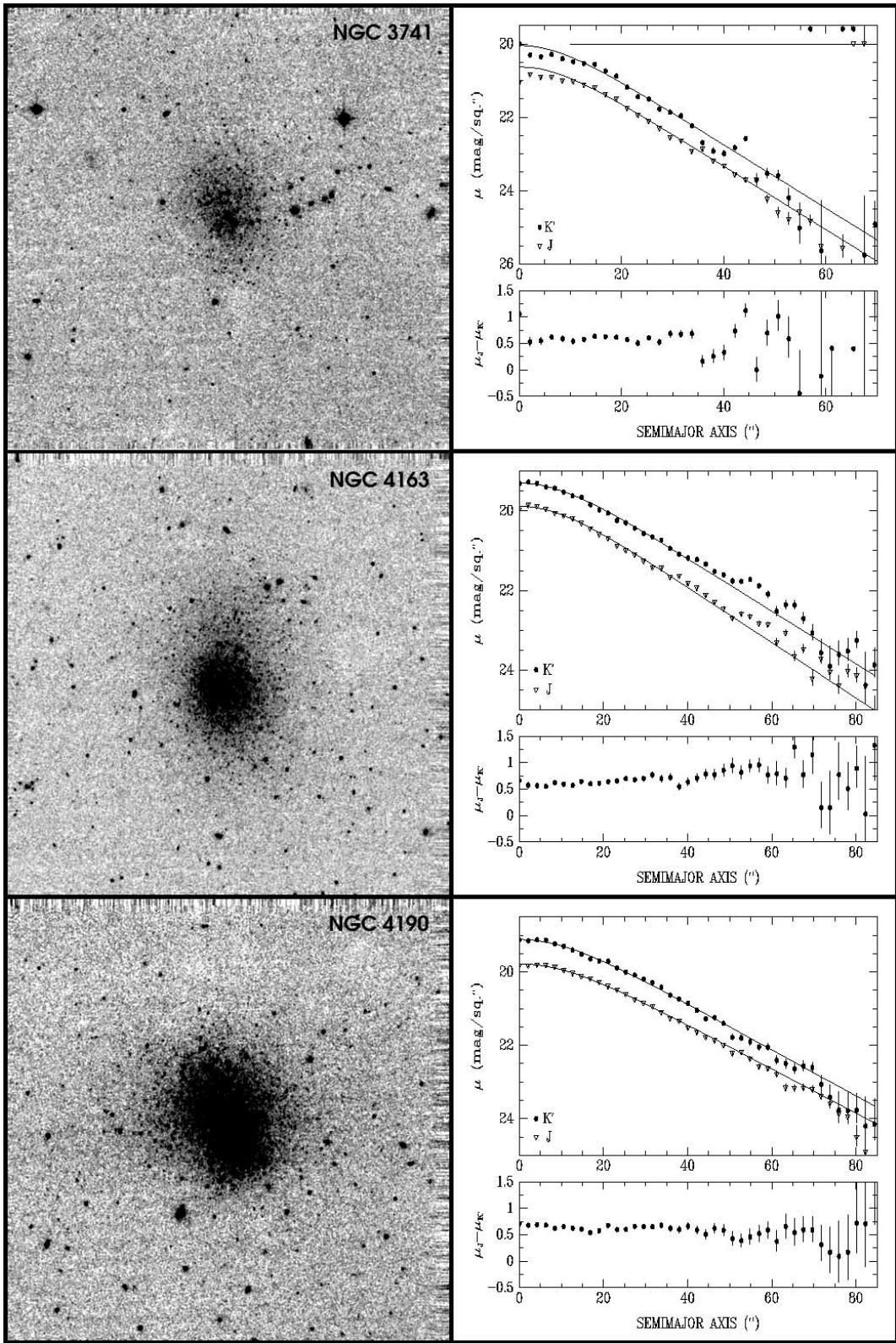


FIG. 1.—Continued

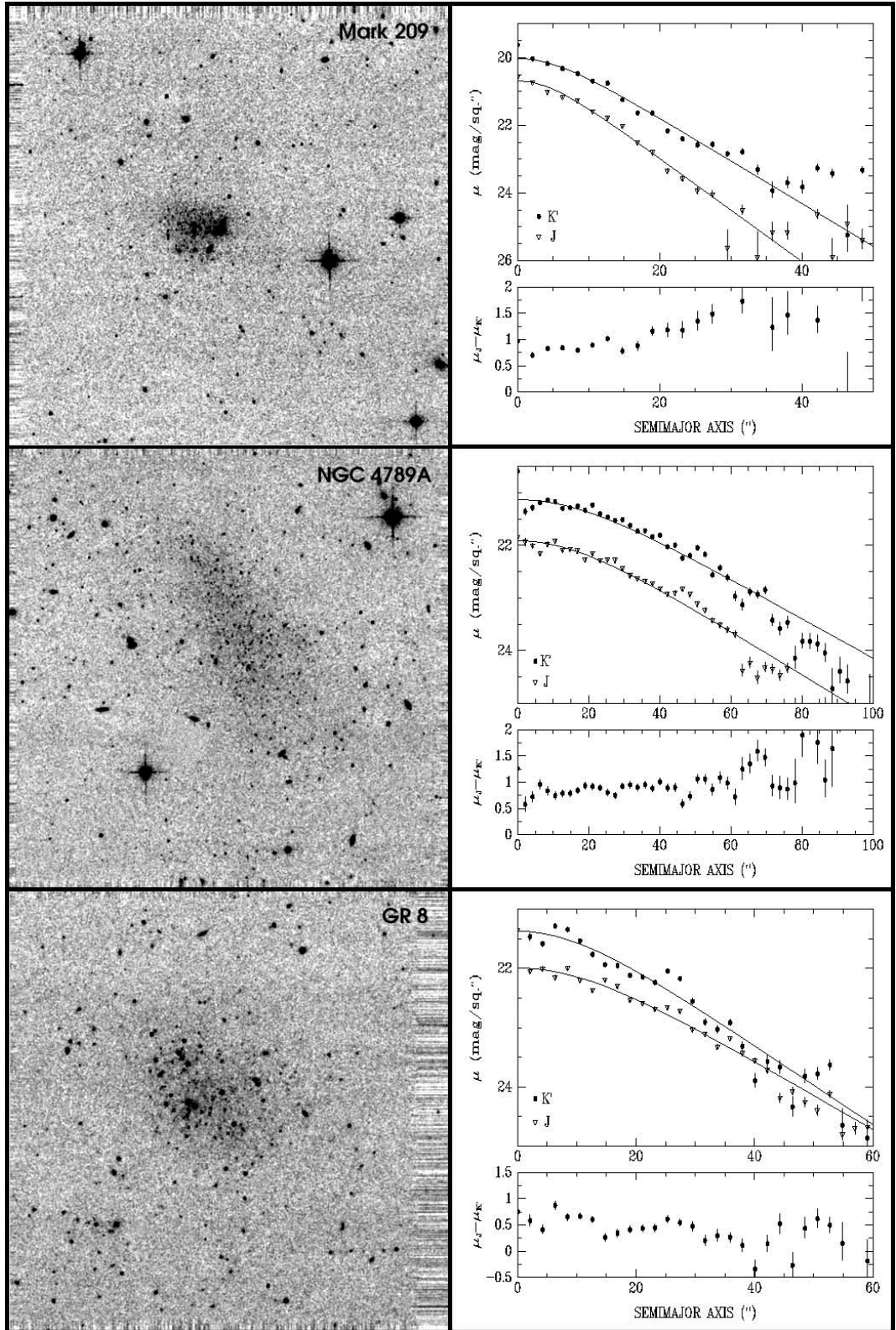


FIG. 1.— *Continued*

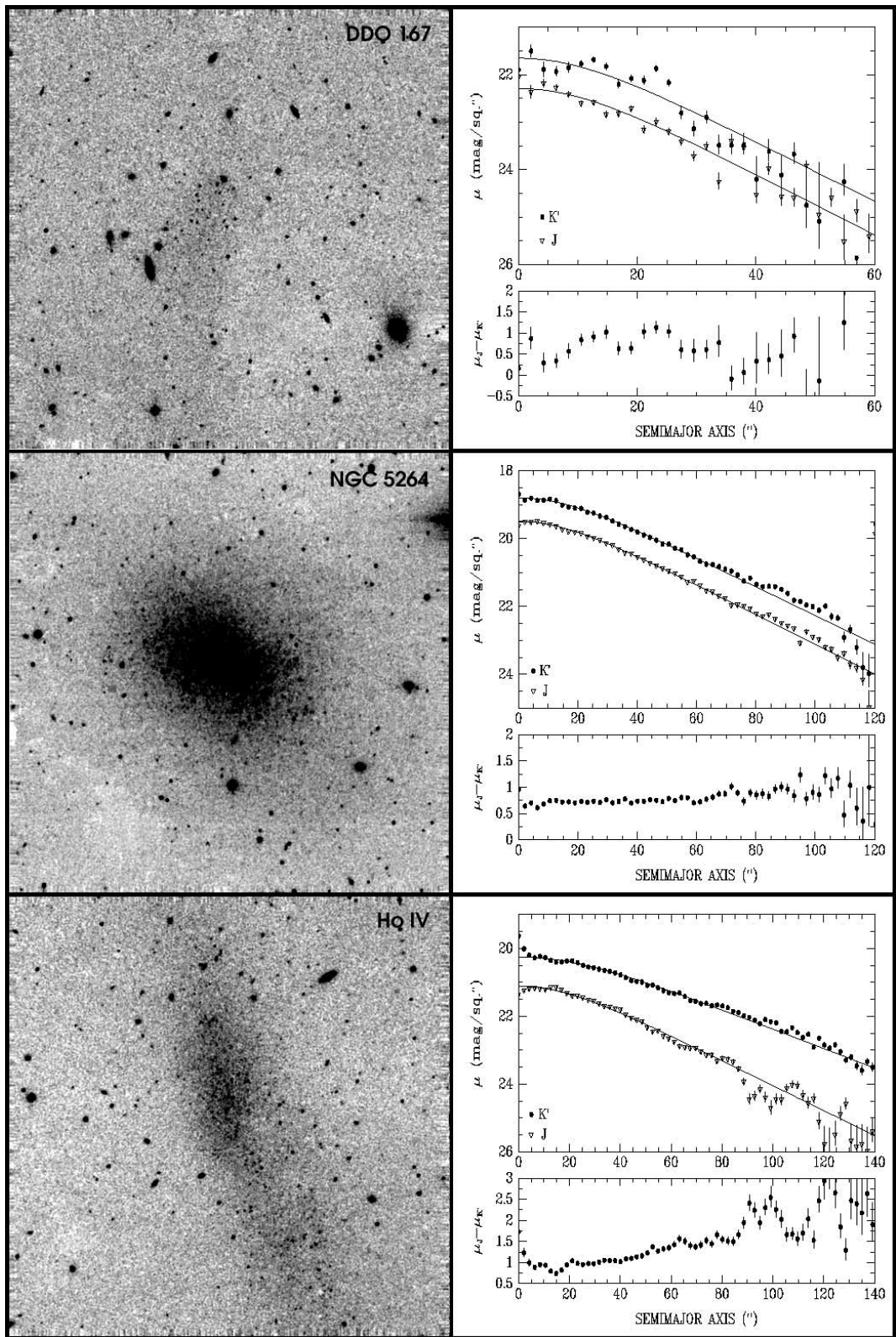


FIG. 1.—Continued

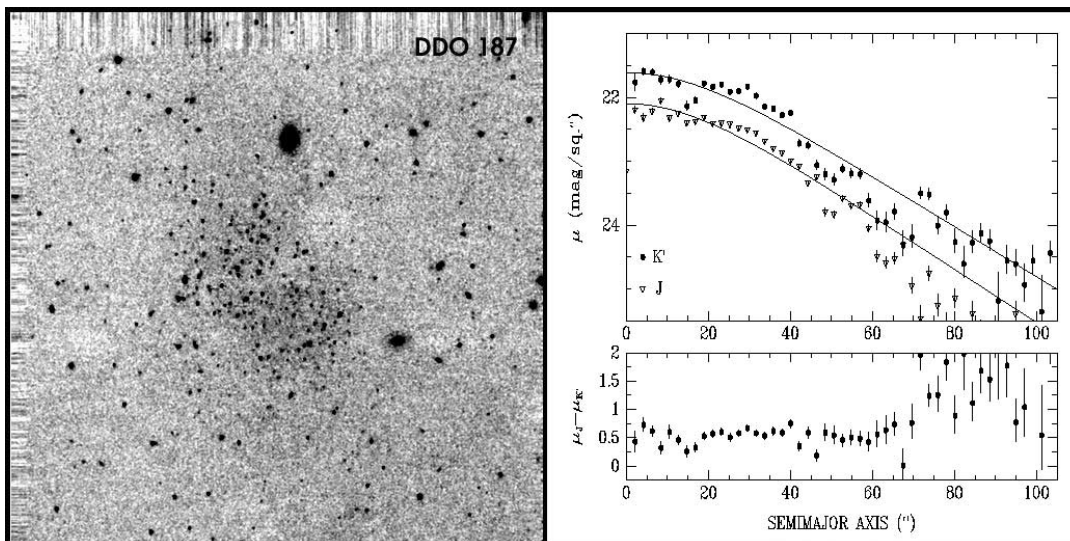


FIG. 1.—Continued

which is equipped with a NICMOS3 256×256 pixel array (Cruz-González et al. 1994). The scale was $0''.85 \text{ pixel}^{-1}$, yielding the same $3'.6 \times 3'.6$ FOV as the CFHT.

Unfortunately, the weather in February–March was unstable throughout the four runs at OAN-SPM (Tapia 2003). We had clear skies for less than half the allocated time, with only one night with photometric conditions. The average seeing was about $2''.5$, but this did not degrade the surface photometry of our targets.

The primary objective of the OAN-SPM runs was to obtain deep imaging of a sample of Virgo BCDs in the NIR, in order to compare their NIR properties with those of field dIs (to be addressed in a future paper). At OAN-SPM we imaged in total 10 dIs from the Local Volume during the first part of the available clear nights. Total exposure times of 20–40 minutes in K_s and 15–20 minutes in J were used at OAN-SPM in order to match the CFHT surface brightness limit, taking into account the ratio of the two apertures (about 3) and the differences in the sky transparency. To obtain these total exposures, we combined individual frames exposed for 1 minute each in both K_s and J .

Due to the larger total exposure time required at OAN-SPM, we sampled the sky half as often as the target. For all our OAN-SPM runs we alternated each sky frame with two target frames, adopting the following observing sequence:

sky-target-target-sky-target-target-sky-. . .-sky-target-target-sky.
(2)

We dithered each galaxy frame by $3''$. The sky frames for each galaxy were observed at positions around the galaxy, $3'–5'$ away.

4. DATA REDUCTIONS

4.1. Overview

One bad pixel map was built for each of our runs using flat-field images taken with two different exposure times. It was applied as the first step in the data reduction process to all CFHT and OAN-SPM raw images (using the *badpix* task of IRAF).

Removal of the background represents the most important step in NIR observations, especially when observing faint extended sources (Vaduvescu & McCall 2004). Without proper care, variations between the sky and the galaxy frames can end

up altering the faint regions of a galaxy, affecting the surface brightness profile (SBP) and total flux. A cleaned sky frame was built for each galaxy frame from neighboring sky frames taken immediately before and after the galaxy frame. The sky frame was then subtracted from the galaxy frame. The reduced galaxy frames were corrected by the flat field, then leveled and median-combined using *imcombine* in order to eliminate hot pixels, cosmic rays, and any “black holes” remaining in the reduced frames due to imperfections in the cleaning of sky frames.

For the image reductions, we used a collection of IRAF scripts named REDNIR.CL. These were written by the first author and tailored to the different observing sequences used at the CFHT and OAN-SPM.⁴

4.2. CFHT Reductions

To generate the flat field, tracked but dithered exposures of the twilight sky were acquired each night and morning. For each filter, a sequence of equal-duration exposures was taken as the twilight brightened or faded. How the signal in any given pixel correlated with the mean for all pixels was used to quantify the relative sensitivity of that pixel to light and thereby generate a flat-field frame.

Often, small extended sources in the background were embedded in raw sky images, 8–10 mag lower than the sky noise. The sky images were also contaminated by bright foreground stars. Vaduvescu & McCall (2004) developed a method to remove these contaminants. Using this algorithm, each pair of raw sky frames straddling a given galaxy frame was used to produce a “cleaned sky frame.” For each raw sky frame, its dithered counterpart was subtracted in order to remove noise and reveal the stars and the extended sources. These sources were detected using DAOPHOT (Stetson 1987, 1992), then cleaned with *imedit*. Finally, the subtracted sky frame was added back, in order to fill in the “black holes” created by stars in the subtraction, generating a cleaned sky frame. The final sky frame was built by averaging the two cleaned sky frames, in order to interpolate in time the background at the time of observation of the galaxy.

Figure 1 presents the reduced K_s images of the 22 field dIs observed at the CFHT that show an unresolved component. The

⁴ The REDNIR.CL NIR image reduction scripts are available at <http://www.geocities.com/ovidiuv/astsoft.html>.

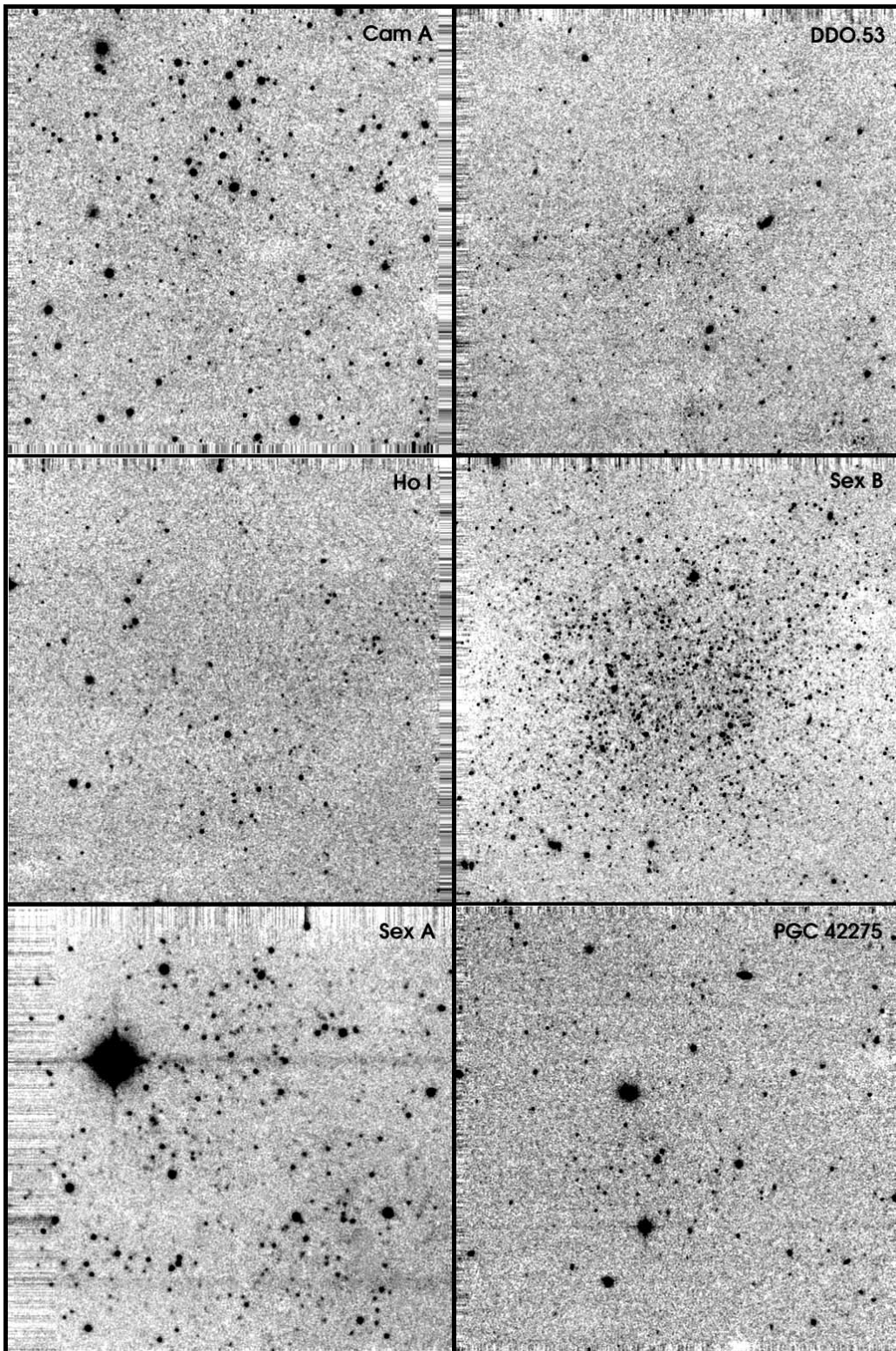


FIG. 2.— K_s images of field dwarf galaxies observed at CFHT larger than the FOV or for which an unresolved component was not detected. North is up and east to the left (FOV is $3'.6 \times 3'.6$, binned 4×4).

mosaic in Figure 2 shows the six galaxies that do not show an unresolved component. For these six galaxies, we were unable to fit light profiles and derive total magnitudes. An additional target (Leo A) was not included in the figure, due to a bright nearby star whose spikes affected the reduced image. This galaxy did not show an unresolved component across the field. In order to emphasize

subtle surface details for display purposes, we binned all frames by 4×4 pixels ($0''.84 \times 0''.84$) using the *boxcar* function in IRAF.

4.3. OAN-SPM Reductions

Due to the smaller aperture of the OAN-SPM telescope, the lower sensitivity of CAMILA, and the higher number of

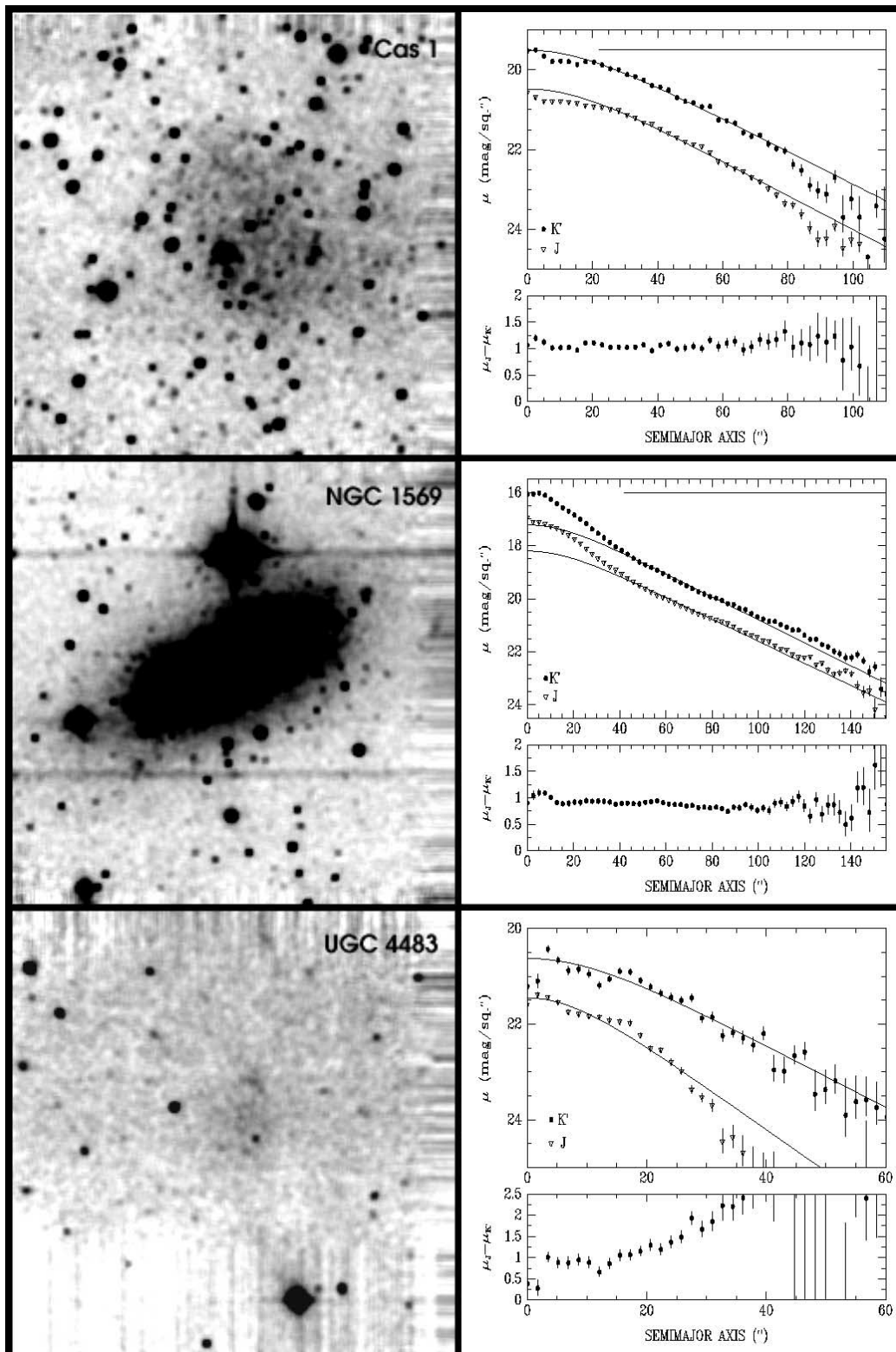


FIG. 3.—Field dwarf galaxies observed at OAN-SPM. *Left panels:* K_s images (north is up and east to the left; FOV is $3'.6 \times 3'.6$). *Right panels:* SBPs in J and K_s (upper plots) and $J - K_s$ color profiles (lower plots).

frames per target (15–40 at OAN-SPM vs. 3–10 at CFHT), we employed a simplified sky-subtraction technique to reduce our OAN-SPM images. We simply subtracted the neighboring sky frame from each galaxy frame, after leveling the signal in the corners to match the signal in the corners of the galaxy frame. Thus, the reduced galaxy frames were leveled us-

ing the corners and median-combined into the final galaxy frame.

For each filter, a flat field was built from a high-signal and a low-signal flat from two series of twilight sky images taken at different illumination levels. The two flats were then subtracted in order to produce the final flat-field image. In Figure 3 we present the

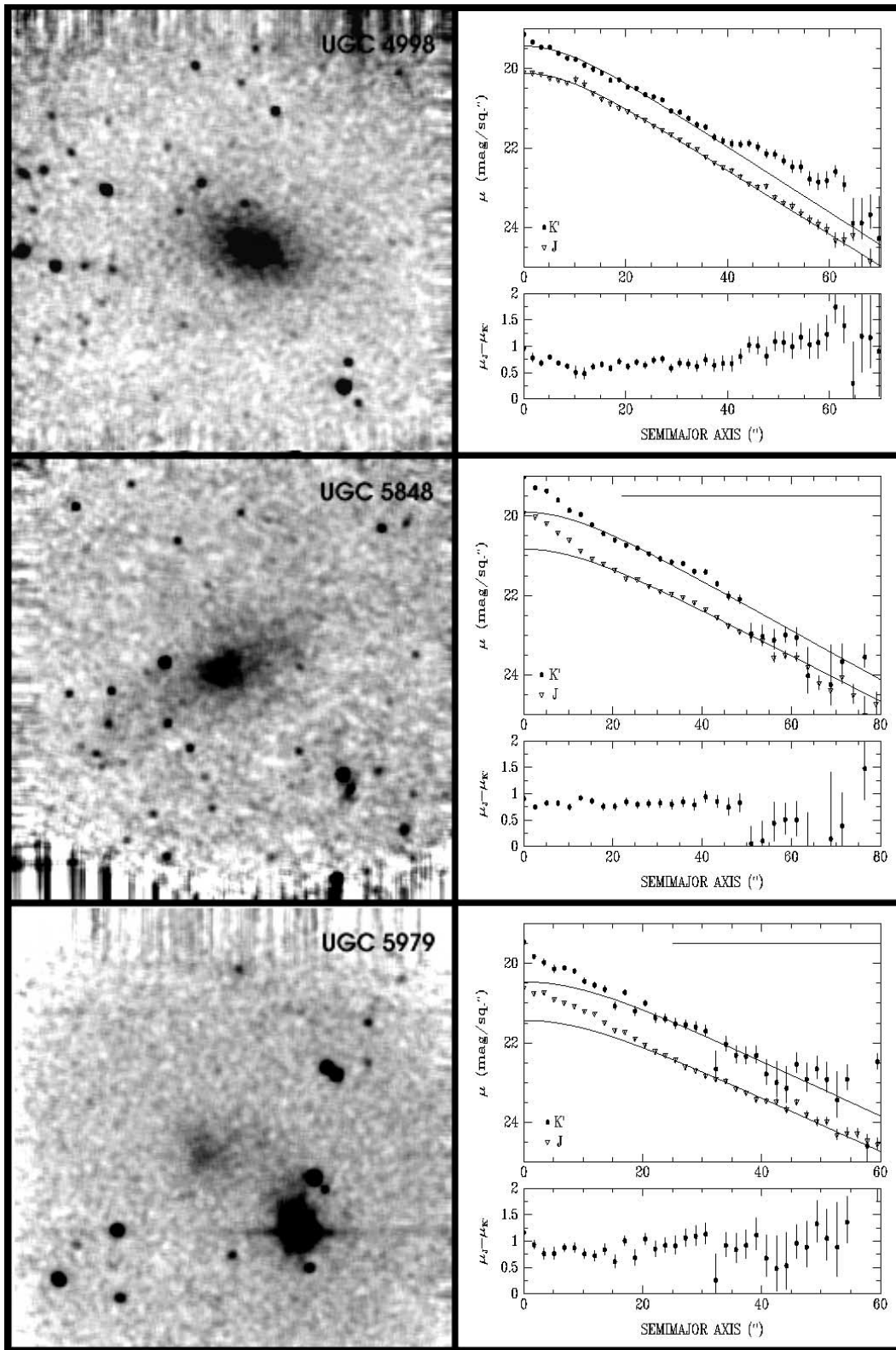


FIG. 3.— *Continued*

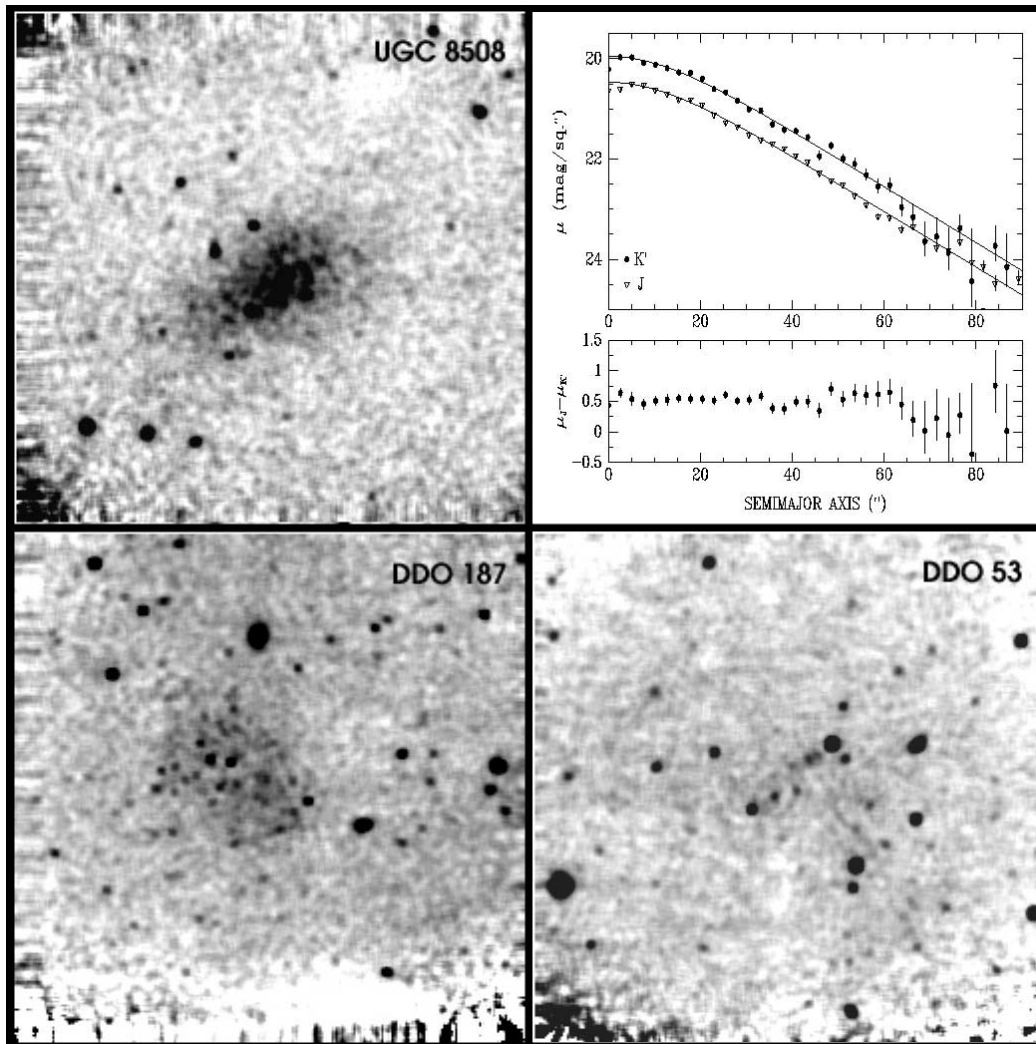


FIG. 3.—Continued

reduced K_s images of the nine field dwarf galaxies observed at OAN-SPM.

5. CALIBRATION OF PHOTOMETRY

5.1. CFHT Photometry Calibration

In 2002 at CFHT we observed four to six Persson standard stars (Persson et al. 1998) at different air masses and times of the night. The sky was photometric on all nights, allowing a determination of the transformation of instrumental magnitudes using observations of these stars. We assumed the following transformation equations:

$$k_S = K_s + k_1 + k_2 X + k_3 (J - K_s), \quad (3)$$

$$j = J + j_1 + j_2 X + j_3 (J - K_s). \quad (4)$$

Here K_s and J stand for the apparent magnitudes in the two bands, k_S and j the instrumental magnitudes, k_1 and j_1 the nightly zero points, k_2 and j_2 the extinction coefficients, and k_3 and j_3 the color coefficients. Using the PHOTCAL package of IRAF, we tried two different approaches to determine the calibration coefficients in equations (3) and (4).

In the first approach, we derived common extinction and color coefficients for the whole run, while determining the individual zero points for each night. The extinction coefficients were

0.065 ± 0.011 and 0.055 ± 0.013 and the color terms were 0.039 ± 0.005 and 0.003 ± 0.005 in K_s and J , respectively. The three nightly zero points agreed within 0.014 mag in K_s and within 0.008 mag in J , while the standard errors in the zero points were less than 0.02 mag for all nights in both bands.

To check the uncertainties, we calculated the zero points for 14 of our science fields using common 2MASS stars appearing in the fields (4–18 stars in each frame). The 2MASS stars were selected using the following conditions:

1. Catalog photometric uncertainties ≤ 0.15 mag (mostly ≤ 0.05 mag).
2. Pointlike appearance on the CFHT images.
3. Magnitudes $K \gtrsim 13$ and residuals $\delta K \lesssim 0.1$ mag.

We found that our original zero points (with only one exception in 28 cases) were higher than the 2MASS ones by an average of 0.31 mag in K_s and 0.24 mag J , reaching a maximum difference of 0.5 mag! To understand the inconsistency, we attempted another approach to derive the calibration coefficients.

In the second approach, solutions for the zero points were decoupled from those for extinction and color coefficients. First, we started by assuming initial values for the extinction coefficients of 0.05 in K_s and 0.11 mag in J for all nights, which are standard figures expected for spring at Mauna Kea (e.g., Manduca & Bell

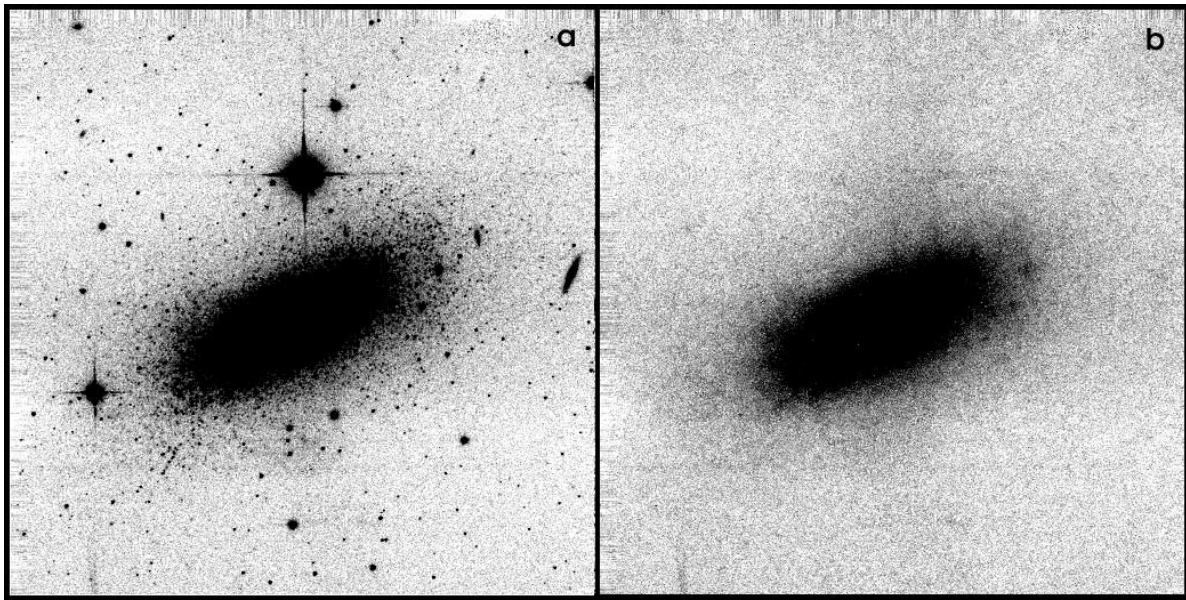


FIG. 4.—(a) K_s image of the dI NGC 1569 observed with the CFHT-IR camera. (b) Unresolved part of NGC 1569, namely, what is left after removing sources with KILLALL. North is up and east to the left (FOV is $3'.6 \times 3'.6$).

1979; Guarnieri et al. 1991). Dropping the color terms, we calculated individual zero points for each standard star and each observation, then their average for each night. Next, we used the estimates for the nightly zero points to calculate average global values for extinction and color coefficients for all three nights. Finally, we used the new estimates of the color coefficients to improve the individual nightly zero points. Note that a similar treatment is suggested as a photometric calibration strategy for 2MASS data.

Using the second approach, we found extinction coefficients of 0.048 ± 0.024 and 0.109 ± 0.025 in K_s and J , respectively, which are very close to the initial values. The color terms were 0.023 ± 0.037 in K_s and 0.022 ± 0.038 in J . The three zero points varied by 0.132 mag in K_s and by 0.162 mag in J . Compared to the 2MASS zero points, our values were higher by an average of 0.04 mag in K_s and 0.08 mag in J . However, the difference was as high as 0.25 mag in one case.

During the 2MASS⁵ survey one calibration field was observed approximately every hour or two each night. Each observation provided six independent measurements of the standard stars. In the first 2 years of the survey, each standard star was measured about 900 times over approximately 50 nights. Based on these data, a global photometric calibration solution was published, which was used to reduce the 2MASS catalog (Nikolaev et al. 2000). Color terms were dropped and global extinction coefficients were calculated by linking data from different nights on a monthly basis. The nightly zero points were assumed to vary linearly with time; see the example in Figure 1 of Nikolaev et al. (2000), in which variations up to about 0.1 mag in range over the night were measured during a given night!

Given the higher frequency with which 2MASS standards were observed and also the compensation for zero-point variability, we decided to adopt the 2MASS frame zero points to reduce all of our CFHT science fields. In seven cases (i.e., DDO 187, Ho IV, NGC 4163, NGC 4190, NGC 4789A, GR 8, and Mrk 209),

when our CFHT frames were sparsely populated by 2MASS stars (fewer than four 2MASS stars per field), we interpolated the zero points using neighboring frames with more stars that were observed within 1 hr of the target, taking care to correct for the difference in the air mass. Note that extinction corrections were small, however, due to both the low air masses (≤ 1.5) at which we observed most of the time and the small atmospheric extinction coefficients.

Based on the scatter in zero points derived from different stars in a given frame, and taking into account the comparison between our second approach and the 2MASS zero points, we expect most of our zero-point errors to be less than 0.05 mag. At maximum, errors may reach 0.1 mag in the following sparsely populated fields, in which we used less than four 2MASS stars:

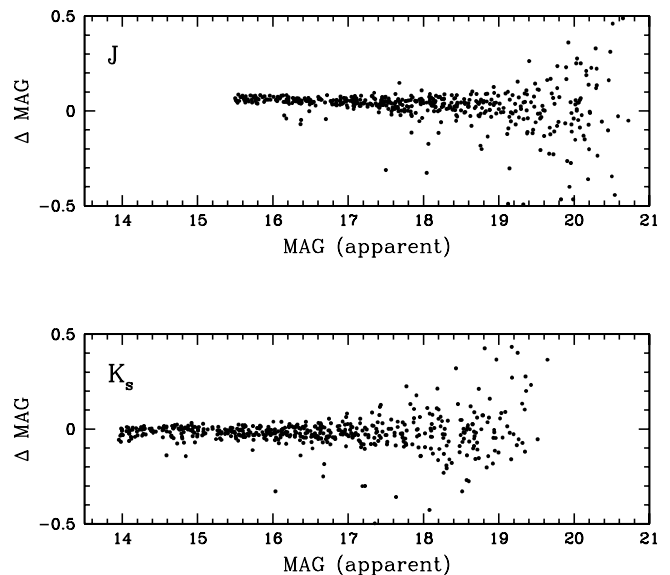


FIG. 5.—Residual magnitudes (recovered — injected) of the recovered stars from the 600 artificial stars added to the image of NGC 1569, plotted as a function of the injected magnitudes.

⁵ See the 2MASS data release documentation by R. Cutri, online at <http://www.ipac.caltech.edu/2mass/releases/docs.html>.

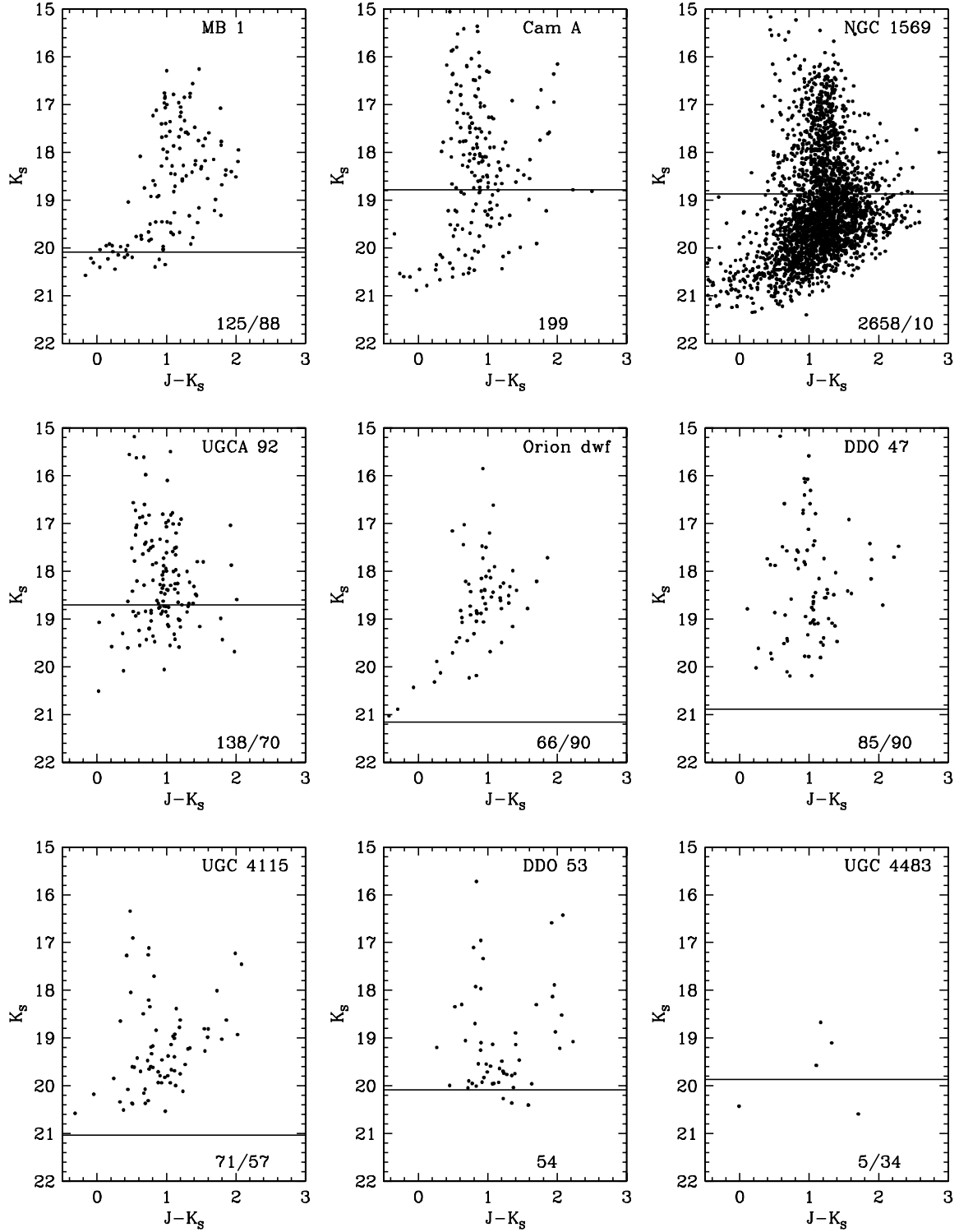


FIG. 6.—CMDs of the resolved stars in the galaxies observed at CFHT. The horizontal solid lines are placed at the apparent K_s magnitude corresponding to $M_{K_s} = -7.5$, taking into account the distance and extinction in Table 2. The first number at the bottom right of each CMD is the number of stars plotted. The second number is the percentage of stars expected to be foreground contaminants. Percentages are not given for galaxies larger than the FOV or showing no unresolved component.

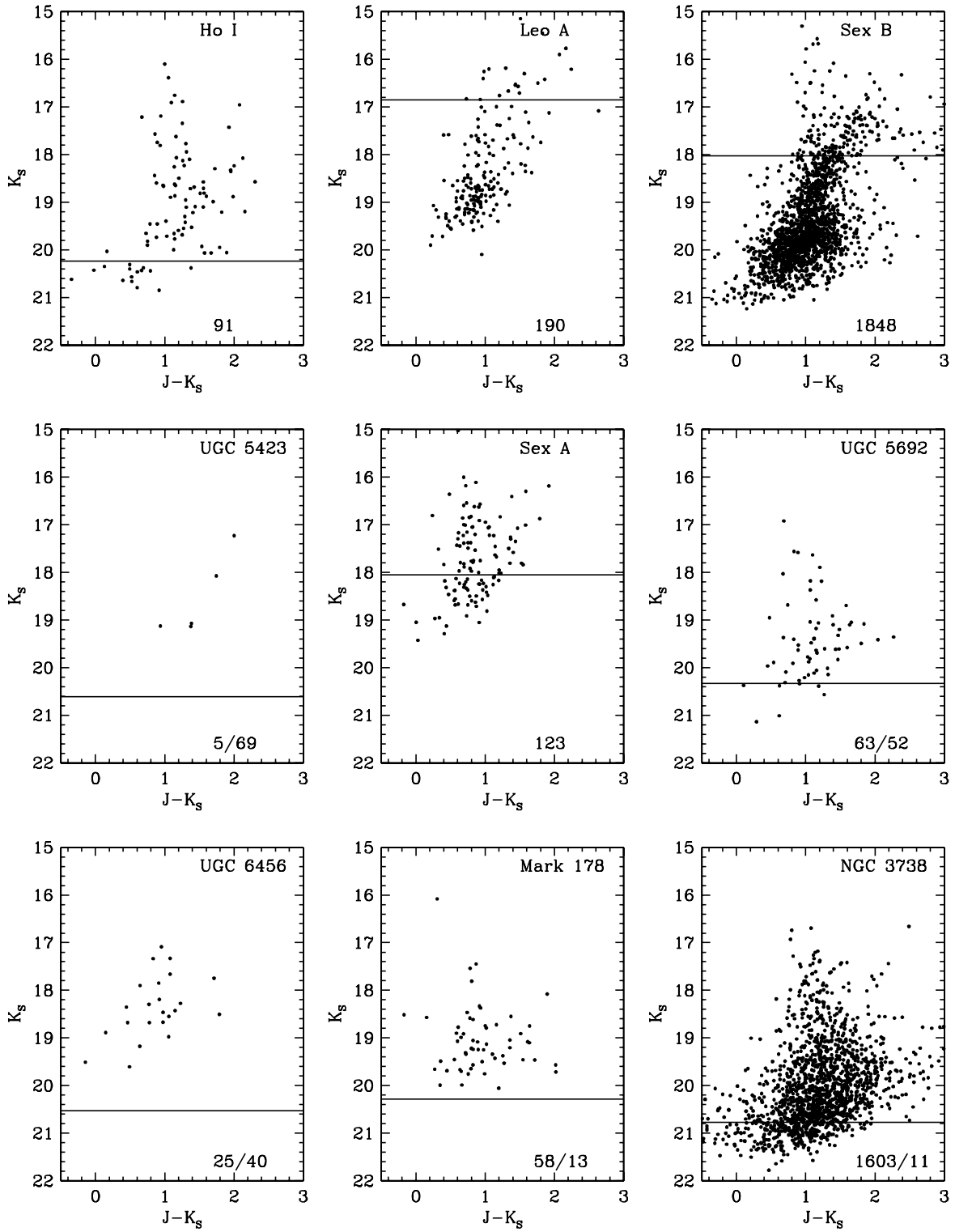


FIG. 6.—Continued

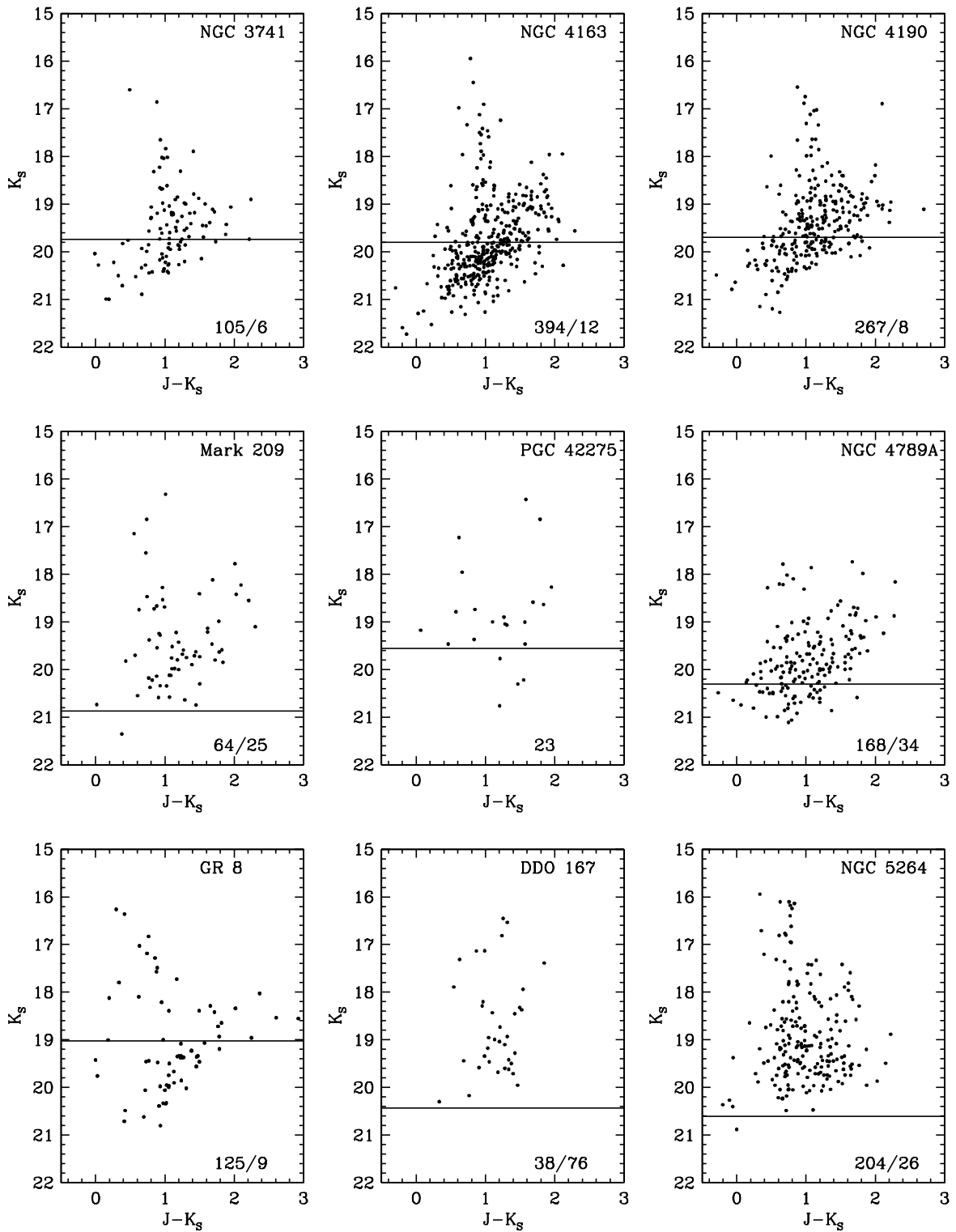


FIG. 6.—Continued

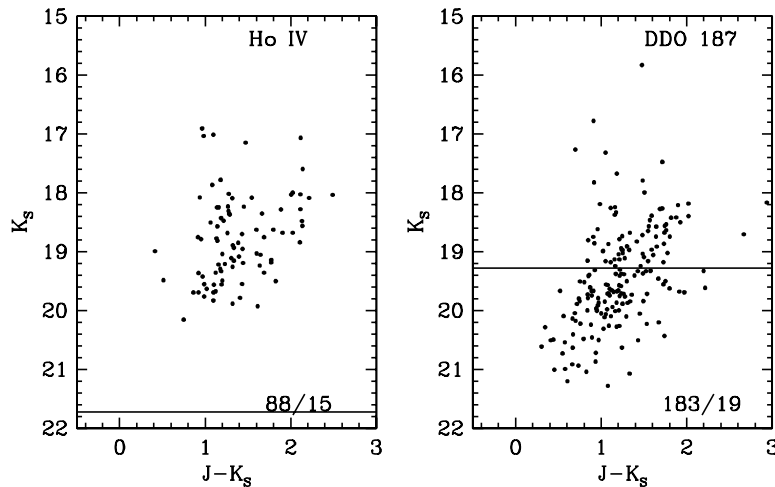


FIG. 6.—Continued

Mrk 178, NGC 4163, NGC 4190, Mrk 209, NGC 4789A, GR 8, Ho IV, and DDO 187.

5.2. OAN-SPM Photometry Calibration

As only one night at OAN-SPM was photometric, the zero points were determined for each frame using common stars observed by 2MASS. We found average residuals of less than 0.04 mag in J and less than 0.07 in K_s for the 3–12 2MASS stars in each field. Based on an error analysis such as that described for CFHT, we conclude that most of our OAN-SPM fields have zero-point errors less than 0.05 mag, with the maximum reaching up to 0.1 mag in four sparsely populated cases: UGC 4998, 5979, 5848, and 8508.

6. STELLAR PHOTOMETRY

As specified above, our CFHT run was tuned to detect AGB stars younger than ~ 8 Gyr, out to 5 Mpc. By resolving the stars to this age limit, we sought to quantify how much the total light represents the old population, which constitutes the bulk of the mass. Due to the much poorer spatial resolution at OAN-SPM, we did not attempt to do stellar photometry based on the OAN-SPM data.

The ratio of the resolved to the total NIR light of a galaxy is a gauge of the contamination of the total light by young stars. To separate the resolved and unresolved components, we used KILLALL, an IRAF script built around the DAOPHOT package, which was developed and used previously in the visible by Buta & McCall (1999). This script iteratively identifies, fits, and removes point sources superposed on a variable background. We applied KILLALL in a three-step process to remove the resolved sources, adopting a threshold level of 5σ for the first two runs and 3σ for the third run. In addition, we employed two point-spread function (PSF) images, the first obtained using an analytic PSF model and the second using a quadratic variable. Finally, a few residuals from bright stars, spikes, and foreground extended sources were cleaned out manually using *imedit*.

KILLALL's final output consists of the following:

1. The unresolved galaxy image.
2. The point-source catalog, which includes all the resolved sources in the frame (i.e., resolved stars in the galaxy, foreground stars, and nuclei of background galaxies).

Figure 4 shows the reduced K_s image of the dI NGC 1569 along with the image of the unresolved component produced by KILLALL.⁶

6.1. Analysis of Crowding and Completeness

In a few galaxies observed at CFHT (NGC 1569, 3738, 4163, 4190, and 5264), the resolved component is crowded, especially near the galaxy centers. Consequently, some stars may be blended and magnitudes may be uncertain. A traditional method to judge the effect of crowding on counts and magnitudes is an artificial star analysis. It was originally developed for the case of a star cluster (Stetson & Harris 1988) and implemented in IRAF under the DAOPHOT package (*addstar* task). One of the most exhaustive analyses was performed by Aparicio & Gallart (1995).

In our application of the method, artificial stars are injected into a reduced galaxy frame (denoted the “real frame”) at random positions. Their randomly assigned magnitudes (named “injected magnitudes”) span a range as wide as that for the real stars measured in the real frame. The resulting frame (denoted the “synthetic frame”) is processed again using KILLALL with the parameters and the PSF image as were used originally. In the presence of crowding, the processing of the synthetic frame recovers only a fraction of the stars present in the real frame, plus some injected stars having measured magnitudes known as “recovered magnitudes.” To evaluate the crowding, the injected and the recovered magnitudes of the injected stars are cross-correlated in order to calculate the number of lost stars and the errors in photometry. The appropriate number of injected stars depends on the stellar density of the area under investigation (i.e., the crowding) and should be a small fraction of the total number of stars detected in the real frame, to avoid self-crowding (e.g., 10%; see Aparicio & Gallart 1995). To improve the statistics, the procedure should be repeated until the total number of injected stars reaches 10 times the number of stars in the real frame.

We injected artificial stars into NGC 1569, the most crowded galaxy of those observed at CFHT. Over the whole frame, we detected 3300 stars in both filters, of which 2658 stars were associated with (within the body of) the galaxy. If the whole frame were filled with stars at a density equal to that within the

⁶ A movie showing the full KILLALL process is available online at http://www.geocities.com/ovidiuv_astro/NGC1569-killall.gif.

TABLE 2
dI SAMPLE

Galaxy (1)	α (J2000.0) (2)	δ (J2000.0) (3)	b (4)	e (5)	P.A. (6)	τ_1 (7)	μ (8)	Method (9)	Reference (10)	W_{20} (11)
Cas 1.....	02 06 05.4	+69 00 12	+7	0.00	0	1.18	27.59	MEM	5	...
MB 1.....	02 35 35.1	+59 22 42	-1	0.60	-66	1.13	27.59	MEM	5	...
Cam A.....	04 25 16.3	+72 48 21	+16	^a	^a	0.25	26.28	TRGB	10	^a
NGC 1569.....	04 30 49.3	+64 50 55	+11	0.45	-64	0.80	26.37	TRGB	17	84
UGCA 92.....	04 32 03.5	+63 36 58	+11	0.50	+51	0.91	26.20	3BS	9	61
Orion dwarf.....	05 45 02.1	+05 04 09	-12	0.60	+29	0.84	28.66	3BS	8	177
DDO 47.....	07 41 55.4	+16 48 09	+19	0.00	0	0.04	28.39	TRGB	15	79
UGC 4115.....	07 57 02.3	+14 23 23	+21	0.60	-39	0.03	28.53	TRGB	15	112
DDO 53.....	08 34 07.2	+66 10 54	+35	^b	^b	0.04	27.58	TRGB	11	^b
UGC 4483.....	08 37 03.4	+69 46 35	+34	0.50	-10	0.04	27.37	TRGB	3	56
UGC 4998.....	09 25 12.4	+68 23 00	+39	0.30	+75	0.07	29.95	SBF	7	...
Ho I.....	09 40 32.3	+71 10 56	+39	^a	^a	0.06	27.74	TRGB	11	^a
Leo A.....	09 59 26.4	+30 44 47	+52	^a	^a	0.02	24.35	TRGB	24	^a
Sextans B.....	10 00 00.1	+05 19 56	+44	^a	^a	0.04	25.53	TRGB	13	^a
UGC 5423.....	10 05 31.0	+70 21 53	+41	0.50	-40	0.09	28.11	3BS	22	67
Sextans A.....	10 11 00.8	-04 41 34	+40	^a	^a	0.05	25.55	TRGB	4	^a
UGC 5692.....	10 30 34.8	+70 37 17	+42	0.30	-19	0.05	27.83	TRGB	11	...
UGC 5848.....	10 44 23.0	+56 25 17	+53	0.40	-65	0.01	29.70	HUB	21	145
UGC 5979.....	10 52 41.1	+67 59 20	+45	0.20	+80	0.02	30.55	HUB	6	104
UGC 6456.....	11 27 59.4	+78 59 37	+37	0.30	0	0.04	28.03	TRGB	20	58
Mrk 178.....	11 33 28.8	+49 14 22	+63	0.50	-49	0.02	27.78	TRGB	14	47
NGC 3738.....	11 35 48.8	+54 31 28	+59	0.30	-24	0.01	28.27	TRGB	14	109
NGC 3741.....	11 36 06.1	+45 17 13	+66	0.26	+23	0.03	27.24	TRGB	14	...
NGC 4163.....	12 12 09.1	+36 10 07	+78	0.30	+11	0.02	27.30	3BS	23	47
NGC 4190.....	12 13 44.4	+36 38 05	+78	0.35	+21	0.03	27.20	3BS	23	67
Mrk 209.....	12 26 17.0	+48 29 39	+68	0.00	+90	0.02	28.37	3BS	18	76
PGC 42275.....	12 38 40.0	+32 46 01	+84	^b	^b	0.02	27.06	3BS	19	^b
NGC 4789A.....	12 54 05.4	+27 08 57	+89	0.60	+26	0.01	27.80	3BS	19	98
GR 8.....	12 58 39.8	+14 13 05	+77	0.20	+61	0.03	26.52	TRGB	2	44
DDO 167.....	13 13 22.7	+46 19 13	+70	0.40	-30	0.01	27.93	TRGB	14	44
UGC 8508.....	13 30 44.4	+54 54 41	+61	0.45	-60	0.02	26.87	TRGB	13	63
NGC 5264.....	13 41 37.0	-29 54 41	+32	0.30	+56	0.06	28.11	TRGB	12	52
Ho IV.....	13 54 46.0	+53 54 20	+61	0.70	+21	0.02	29.22	3BS	16	99
DDO 187.....	14 15 56.5	+23 03 20	+70	0.40	+46	0.03	26.78	TRGB	1	49

NOTES.—Units of right ascension are hours, minutes, and seconds, and units of declination are degrees, arcminutes, and arcseconds. Col. (1): Galaxy name. Col. (2): Right ascension (ellipse fit of the unresolved component in K_s). Col. (3): Declination (idem). Col. (4): Galactic latitude (degrees, from NED). Col. (5): Ellipticity ($1 - b/a$). Col. (6): Position angle (from north to east). Col. (7): Optical depth at $1 \mu\text{m}$ calculated by YES. Col. (8): Distance modulus. Col. (9): Method of determining distance: (MEM) group membership; (TRGB) tip of the red giant branch; (3BS) three brightest blue stars; (SBF) surface brightness fluctuations; (HUB) Hubble law. Col. (10): Reference for distance determinations. Col. (11): Width of the H α line profile measured in km s^{-1} at 20% of the peak.

^a Galaxy larger than FOV.

^b No isophotes detected.

REFERENCES.—(1) Aparicio et al. 2000; (2) Dohm-Palmer et al. 1998; (3) Dolphin et al. 2001; (4) Dolphin et al. 2003; (5) Fingerhut 2002; (6) Huchtmeier & Skillman 1998; (7) Jerjen et al. 2001; (8) Karachentsev & Musella 1996; (9) Karachentsev et al. 1997; (10) Karachentsev et al. 1999; (11) Karachentsev et al. 2002a; (12) Karachentsev et al. 2002b; (13) Karachentsev et al. 2002c; (14) Karachentsev et al. 2003a; (15) Karachentsev et al. 2003b; (16) Makarova 1999; (17) Makarova & Karachentsev 2003; (18) Makarova et al. 1997; (19) Makarova et al. 1998; (20) Méndez et al. 2002; (21) Schneider et al. 1992; (22) Sharina et al. 1999; (23) Tikhonov & Karachentsev 1998; (24) Tolstoy et al. 1998.

area of the galaxy, there would be about 6000 stars in total. Thus, 600 artificial stars (10% of 6000) were injected at a time.

We performed the test for both J and K_s . KILLALL was run once, using a threshold of 5σ and a variable PSF, because most of the artificial stars could be found right from the first step. Most of the 600 stars injected in the synthetic frames were recovered in both filters: 494 stars in J (82%) and 523 stars in K_s (87%). Figure 5 shows the residuals between the recovered magnitudes and the injected magnitudes. Most of the residuals are less than 0.1 mag, the standard deviation being 0.06 mag in K_s and 0.09 mag in J . Comparing these numbers with the standard deviation of the photometry of stars in the real frame (0.14 mag in J and 0.11 mag in K_s), we conclude that crowding has a negligible effect on our photometry.

We also evaluated the degree to which completeness due to crowding varies with radius. First, we selected an ellipse to define the galaxy border, inside of which 252 artificial stars were injected. Altogether, 207 were recovered in J (82%) and 217 in K_s (86%), i.e., almost identical percentages as found across the whole field. Second, we halved the ellipse semimajor axis and repeated the counting. Of the 66 artificial stars injected, 46 stars were recovered in J (70%) and 48 in K_s (73%). We conclude that crowding does not play an important role in our photometry even in the most crowded of the fields in our sample.

6.2. Selected Star Catalog

Many of the stars in the point-source catalog produced by KILLALL are not a part of the galaxy. With the aid of the *pselect*

task of IRAF, a new catalog named the “selected star catalog” was created. Three steps were necessary to build it.

1. In rare cases, bright nuclei associated with known stellar superclusters, such as in NGC 1569, were mistakenly identified by KILLALL as stars. A small ellipse centered on each knot was used to select these nuclei, excluding them from the selected star catalog.

2. Stars superposed on the galaxy image were identified as those point sources located inside the outermost ellipse fitted by the STSDAS *ellipse* task run on the unresolved galaxy image. This step selects the resolved stellar population associated with the galaxy, plus a few foreground stars and artifacts caused by the noise.

3. Milky Way stars residing in the foreground of the galaxy were rejected either by visual inspection (applicable to targets observed at moderate and high latitudes for which very few foreground stars need to be eliminated) or by setting an average limiting magnitude. Bright sources showing a flatter light profile than the stellar PSF, which we associated with possible globular clusters or small background galaxies, were eliminated. Due to the small number of these sources, this step could be performed by visual inspection.

The total flux coming from the resolved part of the galaxy was computed by simply adding the fluxes of all sources in the selected star catalog.

6.3. Color Magnitude Diagrams

For each galaxy, we employed the selected star catalog to build the CMD for the resolved sources. We used the TABLES *tmatch* function of IRAF to match stars. Sources in J and K_s lying within 1 pixel ($0''.211$, i.e., less than half of the average seeing) were paired based on their positions in the two band images and were considered to represent the same star.

Figure 6 presents the CMDs of all galaxies observed at CFHT. In each panel, a horizontal line marks the apparent magnitude corresponding to $K_s = -7.5$ mag, as calculated from the distance modulus listed in Table 2. Three of the 29 galaxies show CMDs with more than 1000 sources, while 15 more have more than 100 stars. In the right corner of each CMD we include two numbers. The first represents the number of stars from the selected star catalog (i.e., thought to be associated with the galaxy). The second number represents the percentage of Milky Way contaminants lying in the foreground of the galaxy. For example, for NGC 1569 there are 2658 resolved stars in the galaxy, of which about 10% are expected to be Milky Way contaminants.

Most of the stars seen in the CMDs have $J - K_s$ colors between 0.6 and 2.0 mag. The CMDs reveal two main features: a blue sequence similar to a vertical finger centered around $J - K_s = 1$ mag and a red tail going as red as $J - K_s = 2.5$ mag. The blue finger is best seen in the CMDs of Cam A, DDO 47, Ho I, NGC 4163, NGC 4190, and NGC 5264. In the CMD of NGC 1569, the base of the blue finger is slightly fainter than an absolute magnitude $K_s = -7.5$ mag, but in Cam A it appears to extend about 2 mag below this luminosity. The red tail is most clearly discerned in the CMD of Sextans B. From the bulk of stars at $(J - K_s, K_s) = (1.0, 20)$, a sequence of stars arises, first tilted toward the upper right, to higher luminosities and redder colors at $(J - K_s, K_s) = (1.8, 17.5)$, then proceeding approximately horizontally to redder colors. Like the blue finger in Cam A, the red tail also begins about 2 mag below an absolute luminosity of $K_s = -7.5$ mag. Other CMDs with evident red tails are Cam A, NGC 4163, NGC 4190, and DDO 187. The first three of these demonstrate that these features are not mutually exclusive.

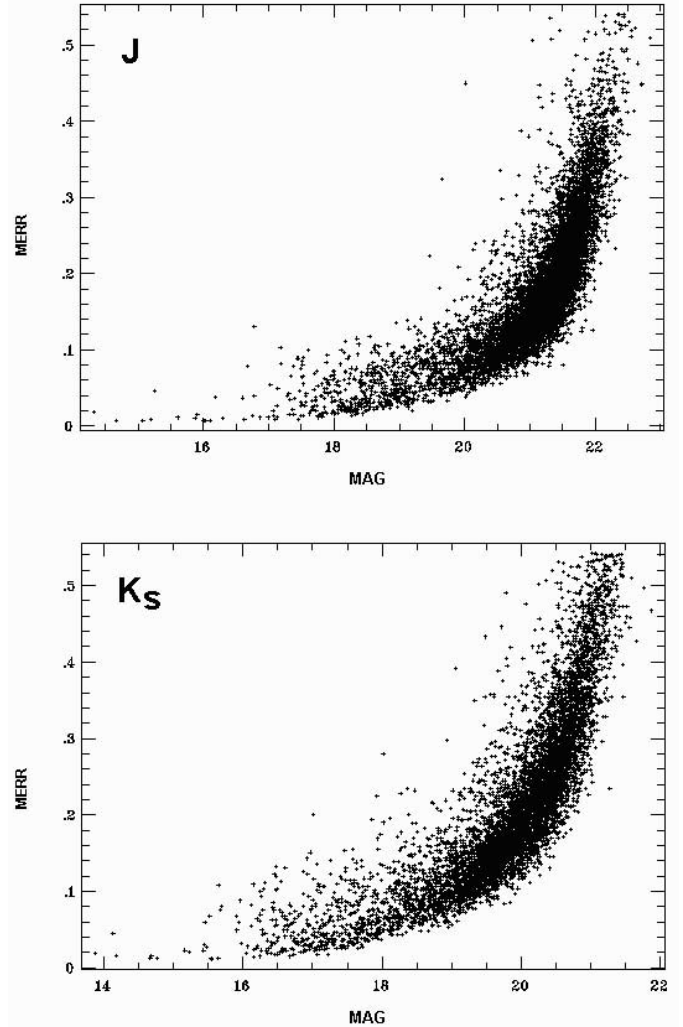


FIG. 7.—Uncertainties in magnitudes for the stars in the selected star catalog for NGC 1569, as a function of apparent magnitude. An average error of about 0.2 mag can be observed in J and about 0.25 mag in K_s , with the maximum reaching about 0.5 mag at the faint end in both bands.

Compared with recent evolutionary models (Girardi et al. 2000; Marigo et al. 2003), the vertical finger agrees with the position of the oxygen-rich intermediate-age and old RGB stars with higher luminosities (plotted as blue dots in Fig. 5b of Marigo et al. [2003]). The red tail, meanwhile, can be associated with the thermally pulsating AGB. As is seen below, the unresolved component has colors very similar to the blue finger in these CMDs (see § 7.6).

The errors in photometry can be evaluated by plotting the formal uncertainties of the magnitudes of stars in the selected star catalogs (listed by DAOPHOT) as a function of the apparent magnitudes. Figure 7 shows the errors for NGC 1569, our most crowded target. Based on this diagram, the average error is about 0.2 mag, with a maximum of about 0.5 mag in both bands at the faint end ($m_J \sim 22$, $m_{K_s} \sim 21$). Similar distributions were observed for the other targets.

Obviously, the contamination of CMDs with Milky Way stars depends on the Galactic latitude b of each field, included in Table 2. A first quantitative approach of the contamination can be done for the targets with latitudes greater than $+20^\circ$. Assuming an average galaxy size corresponding to about 1/3 of the FOV area, the expected number of Galactic contaminants as faint as $K_s = 21$ (about $V = 23$) ranges from 3 to 23 stars (Bahcall &

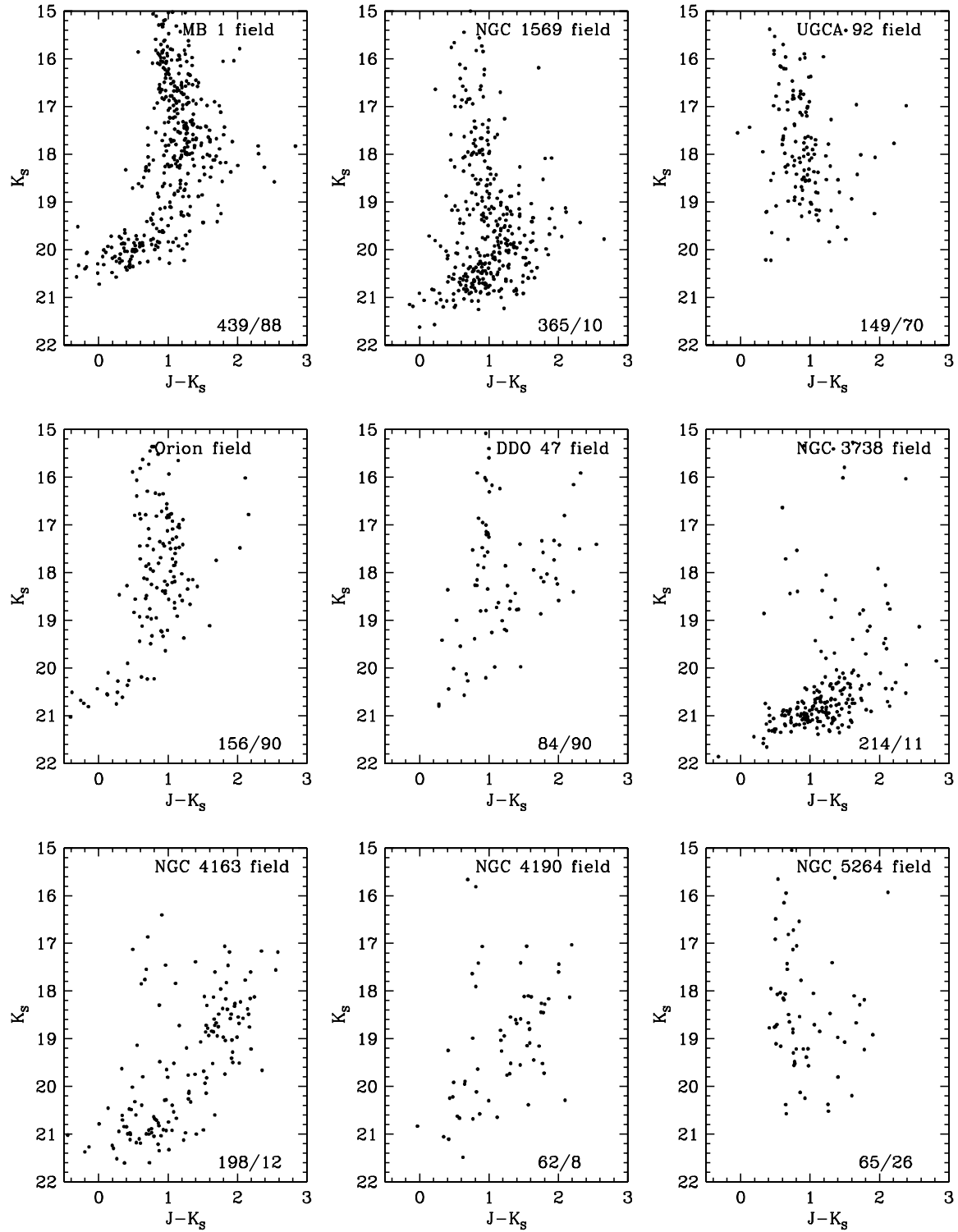


FIG. 8.—CMDs for the stars outside the selected star catalogs (i.e., part of the Milky Way). The first number at the bottom right of each CMD is the number of stars plotted. The second number gives the percentage of the stars expected to be in the foreground (Galactic contaminants), based on the galaxy's area relative to the field area from which the stars plotted here were extracted.

TABLE 3
PHOTOMETRIC PARAMETERS

Galaxy (1)	Filter (2)	Res./Tot. (%) (3)	m_I (mag) (4)	m_r (mag) (5)	m_S (mag) (6)	μ_0 (mag arcsec ⁻²) (7)	r_0 (arcsec) (8)	$r_{22(23)}$ (arcsec) (9)
Cas 1	<i>J</i>	a	11.04	a	10.81	20.49	25.4	76.2
	K_S	a	9.97	a	9.75	19.51	26.3	78.7
MB 1	<i>J</i>	8.4	11.79	11.68	11.67	20.10	22.7	76.2
	K_S	3.1	10.52	10.46	10.40	18.98	24.3	84.3
Cam A.....	<i>J</i>	b	b	b	b	b	b	b
	K_S	b	b	b	b	b	b	b
NGC 1569.....	<i>J</i>	3.4	9.06	8.94	9.37	17.99	21.0	111.7
	K_S	2.7	8.12	8.04	8.45	17.09	21.2	110.8
UGCA 92.....	<i>J</i>	9.9	12.58	12.38	12.27	22.05	37.6	57.3
	K_S	5.0	11.21	11.12	10.82	20.83	41.7	72.8
Orion dwarf.....	<i>J</i>	4.4	11.75	11.70	11.72	20.48	26.3	79.4
	K_S	5.6	10.96	10.90	10.98	19.56	24.3	71.4
DDO 47.....	<i>J</i>	4.1	13.57	13.50	13.38	22.07	16.1	24.3
	K_S	4.6	13.46	13.40	13.36	21.79	14.3	9.1
UGC 4115.....	<i>J</i>	8.3	13.22	13.12	13.10	21.11	18.6	45.2
	K_S	4.3	12.18	12.13	11.94	20.25	21.4	49.1
DDO 53.....	<i>J</i>	c	c	c	c	c	c	c
	K_S	c	c	c	c	c	c	c
UGC 4483.....	<i>J</i>	4.1	14.27	14.14	13.81	21.98	18.0	28.6
	K_S	1.7	13.36	13.33	12.71	20.62	15.9	31.0
UGC 4998.....	<i>J</i>	a	11.85	a	12.01	20.12	13.5	45.3
	K_S	a	11.11	a	11.44	19.43	13.2	40.3
Ho I.....	<i>J</i>	b	b	b	b	b	b	b
	K_S	b	b	b	b	b	b	b
Leo A.....	<i>J</i>	b	b	b	b	b	b	b
	K_S	b	b	b	b	b	b	b
Sextans B.....	<i>J</i>	b	b	b	b	b	b	b
	K_S	b	b	b	b	b	b	b
UGC 5423.....	<i>J</i>	1.2	13.20	13.18	13.07	20.67	13.8	39.1
	K_S	0.5	12.10	12.09	11.97	19.75	15.0	41.5
Sextans A.....	<i>J</i>	b	b	b	b	b	b	b
	K_S	b	b	b	b	b	b	b
UGC 5692.....	<i>J</i>	2.0	10.98	10.96	10.87	20.43	28.8	88.1
	K_S	1.1	10.31	10.29	10.22	19.56	26.0	76.4
UGC 5848.....	<i>J</i>	a	12.34	a	12.35	20.84	19.0	50.7
	K_S	a	11.58	a	11.59	19.90	17.5	45.8
UGC 5979.....	<i>J</i>	a	12.57	a	13.00	21.44	16.1	34.0
	K_S	a	11.66	a	12.06	20.46	15.8	33.0
UGC 6456.....	<i>J</i>	4.5	13.28	13.23	13.44	20.89	10.9	28.7
	K_S	3.2	12.52	12.48	12.54	20.17	11.8	28.0
Mrk 178.....	<i>J</i>	3.2	12.46	12.42	12.35	19.72	12.4	46.1
	K_S	2.3	11.88	11.85	11.74	19.15	12.6	41.9
NGC 3738.....	<i>J</i>	5.8	10.46	10.37	10.54	19.26	19.5	80.7
	K_S	3.7	9.61	9.54	9.68	18.41	19.7	78.7
NGC 3741.....	<i>J</i>	2.9	12.90	12.84	12.81	20.63	12.6	36.1
	K_S	2.7	12.32	12.26	12.22	20.04	12.5	31.3
NGC 4163.....	<i>J</i>	3.0	11.63	11.57	11.66	19.88	15.6	55.5
	K_S	5.8	10.93	10.88	10.96	19.30	16.4	52.1
NGC 4190.....	<i>J</i>	2.7	11.42	11.38	11.32	19.78	18.0	65.8
	K_S	2.9	10.84	10.79	10.74	19.12	17.3	58.0
Mrk 209.....	<i>J</i>	10.0	13.71	13.60	13.77	20.69	7.1	20.1
	K_S	5.7	12.56	12.51	12.70	20.03	8.6	21.6
PGC 42275.....	<i>J</i>	c	c	c	c	c	c	c
	K_S	c	c	c	c	c	c	c
NGC 4789A.....	<i>J</i>	9.3	13.40	13.26	13.15	21.91	26.4	43.7
	K_S	4.8	12.41	12.33	12.17	21.13	28.9	41.5
GR 8.....	<i>J</i>	5.5	13.38	13.29	13.23	22.00	18.7	29.5
	K_S	5.7	13.04	12.90	12.92	21.37	16.2	19.1

TABLE 3—*Continued*

Galaxy (1)	Filter (2)	Res./Tot. (%) (3)	m_I (mag) (4)	m_T (mag) (5)	m_S (mag) (6)	μ_0 (mag arcsec ⁻²) (7)	r_0 (arcsec) (8)	$r_{22(23)}$ (arcsec) (9)
DDO 167.....	J	2.1	13.93	13.91	14.05	22.29	17.0	21.5
	K_s	1.4	13.47	13.45	13.37	21.65	17.3	14.6
UGC 8508.....	J	^a	11.97	^a	12.02	20.47	19.6	59.1
	K_s	^a	11.57	^a	11.44	19.96	19.4	49.9
NGC 5264.....	J	2.5	10.31	10.28	10.26	19.50	24.8	97.3
	K_s	1.5	9.52	9.50	9.48	18.80	25.7	93.6
Ho IV	J	4.8	12.72	12.66	12.43	21.12	29.5	71.3
	K_s	2.9	11.07	11.04	11.03	20.25	37.8	86.5
DDO 187.....	J	4.3	13.08	12.98	12.93	22.10	26.0	37.7
	K_s	9.3	12.60	12.46	12.45	21.72	27.2	5.8

NOTES.—No corrections for Galactic extinction applied. Col. (1): Galaxy name. Col. (2): Filter. Col. (3): Ratio of resolved-to-total flux. Col. (4): Isophotal magnitude of the unresolved component. Col. (5): Total magnitude (unresolved plus resolved). Col. (6): Sech magnitude (from sech law). Col. (7): Central surface brightness (from sech law). Col. (8): Scale length (from sech law). Col. (9): Semimajor axis r_{22} corresponding to $K_s = 22$ mag arcsec⁻² or semimajor axis r_{23} corresponding to $J = 23$ mag arcsec⁻².

^a Observed at OAN-SPM; no stars resolved.

^b Galaxy larger than FOV.

^c No unresolved component detected.

Soneira 1980). More contaminants are expected in the case of our seven galaxies with latitudes lower than $|20^\circ|$.

A more qualitative approach to checking the contamination can be done by considering the CMDs for the field stars selected to lay outside the galaxy, based on its size and shape (i.e., the ellipse center, r_{23} , e , and the position angle [P.A.]). In Figure 8 we present the CMDs for nine galaxies at Galactic latitudes less than $|20^\circ|$ or whose CMDs in Figure 6 show a blue finger, in order to check this feature. The first figure in the right corner of the CMDs in Figure 8 represents the number of stars in the frame that are not part of the selected star catalog (i.e., probably contaminants from the Milky Way). The second number represents the percentage of Milky Way contaminants lying in the foreground of the galaxy (i.e., the same second number as in Fig. 6). The fractions were calculated based on the galaxy area relative to the whole field. Looking at the CMD pairs in Figures 6 and 8 and also at the contamination percentages, the reader can judge the level of contamination in each case.

MB 1 is located in the Galactic plane ($b = -1^\circ$). Despite its relatively large number of selected stars, 88% may be in the foreground, so the CMD has to be regarded with caution. NGC 1569 is located at $b = +11^\circ$. With an expected contamination of about 10%, its CMD in Figure 6 clearly shows a blue finger centered at $J - K_s = 1.2$, which is 0.4 mag redward of the blue finger of the CMD for the field stars in the Milky Way, suggesting that most of the stars bluer than $J - K_s = 1.0$ mag in the CMD of NGC 1569 in Figure 6 are part of the Milky Way. Blue fingers such as that in NGC 1569 have been observed previously in IC 10 by Borissova et al. (2000b). UGCA 92 sits at the same latitude, $b = +11^\circ$, and is a large target; therefore, its contamination may be 70%, and its CMD must be regarded with caution. The Orion dwarf is also situated at a similar low latitude ($b = -12^\circ$), so its expected contamination may be as high as 90%. One of our faintest targets (see Fig. 1), DDO 47, is located at $b = +19^\circ$. Its CMD looks very similar to that of the field; 90% of the stars may be in the foreground. Another well-resolved galaxy, NGC 3738, is located at $b = +59^\circ$ and is expected to suffer only 11% contamination. Its CMD looks different from its field pair, showing no sign of a blue finger. NGC 4163 and NGC 4190 also have high latitudes ($b = +78^\circ$), and their blue fingers at $J - K_s = 1.0$ appear to be largely unaffected by foreground stars. NGC 5264 is located at $b = +32^\circ$. This galaxy is relatively large,

so about 26% of the stars in the CMD may be contaminants, and its blue finger at $J - K_s = 0.8$ may be an artifact.

7. SURFACE PHOTOMETRY

We have measured SBPs and total fluxes coming from the unresolved component of each galaxy via the surface photometry task STSDAS *ellipse*. Working from images cleaned of stars (via KILLALL) instead of the original frames, our measurements have the huge advantage of being unaffected by surface brightness fluctuations (SBFs) due to inclusion of light from the resolved sources, which can be significant for bright stars.

Two galaxy frames observed at OAN-SPM (Cas 1 and NGC 1569) included more than 100 stars in their fields. Their resolved and unresolved components were separated using KILLALL. The other five OAN-SPM frames (UGC 4483, 4998, 5848, 5979, and 8508) showed very few stars, so we were unable to use KILLALL, as we were unable to construct reliable PSFs. For these five cases, we simply used *imedit* to manually remove the stars in the frames.

7.1. The Unresolved Component

Unresolved images of the faintest galaxies were binned at 5×5 pixels ($1'' \times 1''$) in order to improve the signal-to-noise ratio. Following this process, 20 out of the 29 dwarfs observed at CFHT showed an unresolved component.

In order to measure SBPs, we used the ISOPHOT *ellipse* task on the cleaned K_s images in two stages. First, we guessed the initial ellipse centers, ellipticities, and position angles but allowed them to vary freely with radius. Then we plotted the fits using the *isopall* task and improved the ellipse parameters by analyzing the outer isophotes, where the underlying old component is expected to set the geometry of the galaxy. Second, we fixed the center, ellipticity, and position angle and repeated the fitting process. By allowing only the surface brightness to vary with radius, it was possible to measure isophotes to fainter levels than in the first stage.

The upper graphs in the right panel beside each galaxy in Figures 1 and 3 present the SBPs in K_s and J for the unresolved component of the galaxies observed at CFHT and OAN-SPM, respectively. The formal uncertainties in the surface photometry as given by *ellipse* are plotted as error bars. Most of the errors are less than 0.1 mag arcsec⁻².

TABLE 4
COMPARISON WITH 2MASS

Galaxy (1)	$\Delta\alpha$ (arcsec) (2)	$\Delta\delta$ (arcsec) (3)	Δe (4)	Δ P.A. (deg) (5)	Δm_J (mag) (6)	Δm_K (mag) (7)
NGC 1569.....	-2.2	-2.4	+0.09	+1.8	-0.11	-0.16
NGC 5264.....	-5.0	-6.3	+0.00	+14.0	+1.06	+1.32
NGC 4190.....	-4.2	-12.1	+0.41	+9.0	+1.67	+1.75
NGC 4789A.....	-2.5	+1.5	-0.60	+63.8	+2.98	+1.53

NOTES.—Col. (1): Galaxy name. Col. (2): Difference in right ascension (2MASS minus ours). Col. (3): Difference in declination (idem). Col. (4): Difference in ellipticity (idem). Col. (5): Difference in position angle (idem). Col. (6): Difference in total magnitude J (idem). Col. (7): Difference in total magnitude K_s (idem).

Table 2 gives the adopted values of the ellipticity (e) and major-axis position angle (P.A.) from which the profiles were derived. Ellipticity errors listed by *ellipse* are less than 0.05 in most cases, and position angles are uncertain to about 2° . For the faint targets (DDO 47, DDO 167, DDO 187, UGC 4483, UGC 5979, UGC 6456, and NGC 4789A), we estimate that errors reach 0.1 in ellipticity and 5° – 10° in position angle.

7.2. Isophotal and Total Magnitudes

We define the isophotal magnitude (m_I) of each galaxy to be the total flux of the unresolved component. The isophotal magnitudes are given by the instrumental detection limit as the total flux integrated to the faintest isophote. The detection limits were $\mu_{K_s} = 23$ mag arcsec $^{-2}$ and $\mu_J = 24$ mag arcsec $^{-2}$ for both facilities. We employed *isoplot* to plot the magnitude growth curves, which at large radii converge asymptotically to the isophotal magnitudes. By adding the flux of the unresolved component to the flux of the resolved population (summed from all stars in the selected star catalog), we obtain the total magnitude (m_T). The isophotal and total magnitudes are listed in Table 3. The differences between the two are very small; less than 0.1 mag in most cases with a maximum of 0.2 mag in a few cases. This reveals the small contribution of the resolved sources to the total light from the galaxies, which is discussed further in § 8.1.

Only four galaxies from our sample were detected by 2MASS.⁷ In Table 4 we compare measurements by listing the differences in the total magnitudes, Δm_J and Δm_{K_s} , ellipticity, Δe , and position angle, Δ P.A. (2MASS minus our values). We list the four targets in order of descending total luminosity. NGC 1569, the brightest galaxy, shows the smallest differences, with the 2MASS total magnitude being brighter by only ~ 0.1 mag. The small difference may be due to imperfect removal of the bright foreground star 2MASS 04304867+6451504 ($K_s \sim 7.5$ mag) located just $\sim 1'$ north of the galaxy. The other three galaxies are fainter and show increasing residuals in their total magnitudes, averaging about 1.5 mag and going in one case as high as 3 mag. In all three cases 2MASS underestimates the fluxes, likely because of the brighter detection limit.

We observed NGC 1569 at both CFHT and OAN-SPM, allowing for a comparison between our two sets of results. The differences between the CFHT values and the OAN-SPM values are $\Delta e = -0.05$, Δ P.A. = $+5^\circ$, $\Delta m_J = +0.03$ mag, and $\Delta m_{K_s} = +0.02$ mag. Agreement is outstanding.

A critical factor affecting photometry is the level of the sky. Our observing and reduction strategies removed sky to an ac-

curacy of 0.02% in K_s relative to the original signal, as we combined galaxy frames from which we subtracted appropriate sky frames close in time and position. In addition, for the small galaxies the sky level was checked by computing the median over the whole field and then adjusted additively to 0. For the large galaxies, it was checked using the average of the medians in the corners. Thus, we believe that the uncertainties in the isophotal magnitudes are determined mainly by the zero points, whose typical errors are less than 0.1 mag (see § 5).

Uncertainties in the total magnitudes include the errors in the isophotal magnitudes (for the unresolved component) and the formal errors in fluxes in the selected star catalogs. The former are about 0.1 mag, as specified above. The latter mostly cancel out statistically due to the large number of stars detected in each galaxy.

Throughout this paper we have not corrected our magnitudes and colors for extinction and reddening, which are expected to be less than 0.05 mag for most of the dIs but which may amount to 0.38 mag extinction for MB 1, which is at $b = -1^\circ$. We plan to examine these effects in a future paper that will enlarge our dI sample.

7.3. Astrometry

We measured the International Celestial Reference System J2000.0 absolute positions of the galaxy centers, which were derived using the unresolved galaxy images. For all galaxies except four, the reference stars were exclusively 2MASS catalog stars. For the four remaining frames with only one or two 2MASS stars in the FOV, we completed the reference system with a few Guide Star Catalog, version 2.2, or USNO-B1 positions. The absolute J2000.0 positions are listed in Table 2.

Two sources are responsible for the uncertainties in galaxy positions listed in Table 2: the reference system and the ellipse centering algorithm. The astrometric accuracy of the 2MASS Point Source Catalog for stars with magnitudes in the range of $9 \leq K_s \leq 14$ is about $0''.07$ – $0''.08$, reaching $0''.2$ – $0''.3$ for its faintest sources.⁸ The 2MASS observing epoch (1997–2001) is very close to our runs (2001–2004), so proper motions of the faint stars used for our reference fields do not affect our positions by more than $\sim 0''.1$.

As described previously, the fitting of the unresolved component was done in two steps, in the first allowing the center, ellipticity, and position angle of the isophotes to be free parameters, while in the second fixing them at values found for the outer regions. In the second step, the errors in the centers came out to be less than $\sim 0''.5$. Therefore, we can adopt $1''$ as the maximum error in astrometry for most of our targets.

7.4. Profile Fitting

James (1991, 1994) pioneered NIR surface photometry (J , H , and K_s) of dwarf galaxies. He modeled SBPs with an exponential law for dIs and BCDs and a de Vaucouleurs $r^{1/4}$ law for dEs. Bergvall et al. (1999) employed a pure exponential profile in order to fit the disks of a sample of low surface brightness blue galaxies observed in J , H , and K_s . Patterson & Thuan (1996) used an exponential law with an inner limit in radius in order to fit the underlying component of a sample of 51 dwarfs (mostly dIs) observed in the visible.

A combination of two or three different models has been employed by some authors to improve the fits to the SBPs. Gavazzi et al. (2000) used the exponential law, the de Vaucouleurs law, or

⁷ See the 2MASS GATOR Catalog at <http://irsa.ipac.caltech.edu/applications/Gator>.

⁸ See footnote 5.

a combination of the two in order to fit the light profiles for dIs and BCDs observed in H and K_s in five nearby clusters. Gavazzi et al. (2001) employed a de Vaucouleurs law, an exponential law, a “mixed” profile (sum of the two), and a “truncated” profile (a blend of the two defined by a critical radius). This latter work was based on H -band observations of 75 faint galaxies, mostly dEs in the Virgo Cluster. Using observations in the visible of 12 BCDs and two other bright starburst galaxies, Papaderos et al. (1996) decomposed SBPs into three components: an exponential at large radius, a plateau at intermediate radius, and a Gaussian at small radius.

As mentioned previously, we derived our SBPs using the *ellipse* task of the ISOPHOT package in IRAF. Most of the SBPs show a flattened core and exponential component extending down to a surface brightness of about $\mu_{K_s} = 23$ mag arcsec $^{-2}$ and $\mu_J = 24$ mag arcsec $^{-2}$, as can be seen in Figures 1 and 3.

We attempted to fit our SBPs over the entire length of the semimajor axes using an exponential or a plateau component, either alone or as a sum. These attempts failed to provide good fits at both small and large radii. Given that we were especially interested in properly characterizing the outer regions, where we believe that the old stellar population dominates, we looked at a variety of other functions to simultaneously fit both the inner and outer regions. Good fits could be achieved for most galaxies using a hyperbolic secant function,

$$I = I_0 \operatorname{sech} \frac{r}{r_0} = \frac{I_0}{\cosh(r/r_0)} = \frac{2I_0}{e^{r/r_0} + e^{-r/r_0}}. \quad (5)$$

Here I represents the fitted flux at radius r , defined as the distance from the center along the semimajor axis, I_0 is the central intensity (expressed in counts pixel $^{-1}$), and r_0 represents the scale length of the profile (expressed in pixels).

A hyperbolic secant was previously employed by van der Kruit & Searle (1981). The authors used the function sech^2 to model the vertical distribution of light in galactic disks based on dynamical expectations for an isothermal disk.

In magnitude units, the fit is given by

$$\begin{aligned} \mu &= \text{zp}_s - 2.5 \log I = \text{zp}_s - 2.5 \log \left(I_0 \operatorname{sech} \frac{r}{r_0} \right) \\ &= \text{zp}_s - 2.5 \log \frac{I_0}{\cosh(r/r_0)}, \end{aligned} \quad (6)$$

where zp_s represents the zero point of the surface brightness magnitude system. At larger radii, equation (6) is convergent to the sech magnitude (m_s), while curving and leveling out at near-zero radii toward the central surface brightness (μ_0). Expressed in mag arcsec $^{-2}$, the central surface brightness is simply

$$\mu_0 = \text{zp}_s - 2.5 \log I_0. \quad (7)$$

To perform the actual fitting of the SBPs generated by *ellipse*, we employed the task *nfit1d* (in the FITTING package of STSDAS), entering equation (5) as our user specified function for the USERPAR/FUNCTION parameter. For plotting purposes, fitted fluxes were converted into mag arcsec $^{-2}$ using the zero points for the frames. We have plotted the fits on top of the SBPs in the upper graphs in the right panels of Figures 1 and 3.

In a few cases (NGC 1569, NGC 3738, UGC 5848, and UGC 5979), the SBPs show some excess flux at small radii. This could be evidence of starburst activity near the galaxy center, which

has been previously suggested for NGC 1569 (Greggio et al. 1998; Aloisi et al. 2001) and NGC 3738 (Hunter et al. 1980; Karachentsev et al. 2003a). A few other cases (Mrk 178, NGC 3741, and Cas 1) present some flux deficits at small radii. When necessary, to prevent results from being biased by flux excesses or deficits at small radii, we restricted fits to the outer regions. For those galaxies for which this was done, we plotted the fitting interval as a line in the upper part of the graphs in Figures 1 and 3. Table 3 lists the central surface brightness μ_0 (in mag arcsec $^{-2}$) and the scale length r_0 (in arcseconds) in both J and K_s . For most galaxies, the scale lengths in J and K_s agree to within about $1''$.

7.5. Sech Magnitudes, Semimajor Radius

The “sech magnitude” of the fit to the unresolved component of each galaxy can be calculated from equation (5). Let a and b be the semimajor and semiminor axes of the isophotes, e the ellipticity, and $I(a)$ the average surface brightness in an elliptical annulus with area dA . Then,

$$dA = d(\pi ab) = d[\pi a^2(1 - e)] = 2\pi a(1 - e) da, \quad (8)$$

and the total flux F is given by

$$F = \int_0^\infty I(a) dA = 2\pi(1 - e) I_0 \int_0^\infty a \operatorname{sech}(a/R_0) da. \quad (9)$$

By substituting $x = a/r_0$ in the last integral, the integrated (sech) flux becomes

$$F = 2\pi I_0 r_0^2 (1 - e) \int_0^\infty x \operatorname{sech} x dx. \quad (10)$$

The integral on the right side cannot be resolved analytically. Using MAPLE, we obtained a numerical approximation of 1.83193119. With this result, the sech magnitudes can be calculated from

$$m_s = \text{zp}_s - 2.5 \log [11.51036 I_0 r_0^2 (1 - e)], \quad (11)$$

with zp_s representing the frame zero point for point sources.

We include in Table 3 the sech magnitudes (m_s) for the unresolved component of the galaxies as calculated from equation (11). Most sech magnitudes are very close to the isophotal magnitudes (in most cases within 0.2 mag). In only four cases do the discrepancies between m_s and m_I reach 0.4 mag, due to the faintness of the unresolved component or the presence of a starburst (NGC 1569). Figure 9 plots the difference between the isophotal magnitude m_I and the sech magnitude m_s as a function of m_I .

Using equation (6) we have calculated the semimajor axis r_{22} corresponding to $\mu_{K_s} = 22$, as well as r_{23} , corresponding to $\mu_J = 23$ mag arcsec $^{-2}$. The positive solution for the second-order equation in r_{22} comes to

$$r_{22} = r_0 \ln \frac{1 + \sqrt{1 - A_{22}^2}}{A_{22}}, \quad (12)$$

where A_{22} is given by

$$\log A_{22} = \frac{\text{zp}_s - 22 - 2.5 \log I_0}{2.5}. \quad (13)$$

There are similar formulae for r_{23} . Our values for r_{22} and r_{23} are listed in Table 3.

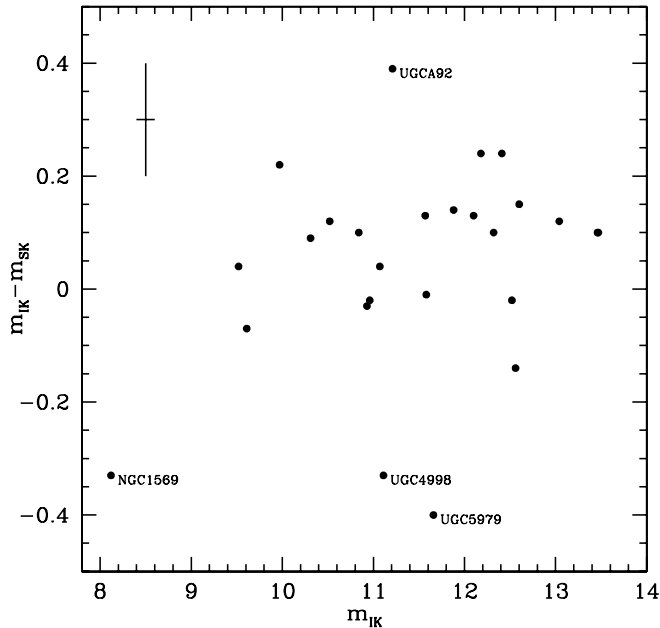


FIG. 9.—Residuals between the isophotal magnitudes m_I and the sech magnitudes m_S , showing the goodness of the sech fit to the SBPs in K_s . The three UGC galaxies are faint, while NGC 1569 has an anomalously bright core due to its starburst. All other unresolved components could be fitted within 0.2 mag in total magnitude.

Based on the *nfit1d* rms error analysis, we evaluate the typical uncertainties in r_0 , r_{22} , and r_{23} to be about 2% and the uncertainties in the central surface brightness μ_0 and the sech magnitude m_S to be less than ~ 0.1 mag arcsec $^{-2}$ and ~ 0.1 mag, respectively. From a purely empirical point of view, the estimated uncertainty of 0.1 mag in m_S agrees reasonably well with most of the galaxies plotted in Figure 9, which show $m_I - m_S \lesssim 0.1$.

7.6. Color Profiles

Color profiles for the underlying unresolved component of each galaxy can be plotted by combining the J and K_s surface brightnesses via the *tealc* task of TABLES. For each galaxy the color profile is given in Figures 1 and 3 as the bottom graph of the right panels beside the picture. Most galaxies show a remarkably constant $J - K_s = 0.8$ – 1.0 mag, close to the color of the blue finger seen in the CMDs.

8. NIR PROPERTIES OF dIs

8.1. Resolved/Total Flux Ratios

The brightest stars in dwarfs are relatively young, so the ratio of the resolved flux to the total flux gives some idea of how well the total light reflects the mass of the old population. We define the resolved flux as the sum of the fluxes of the stars detected by KILLALL down to $M_{K_s} = -7.5$. We deliberately do not include all resolved sources in the resolved flux, since our detection limit for resolved sources varies from one object to another, based on their distances. Indeed, we include only those sources brighter than $M_K = -7.5$ mag, since our observations were tuned to detect such sources in all galaxies. The total flux is defined as the flux of the unresolved component plus the sum of the fluxes of all resolved sources (faint stars), regardless of brightness. The ratio of the resolved to the total flux is denoted here as “resolved/total.”

In order to check the sensitivity of the results to resolution, we degraded the resolution of GR 8 by a factor of 2, as if its distance

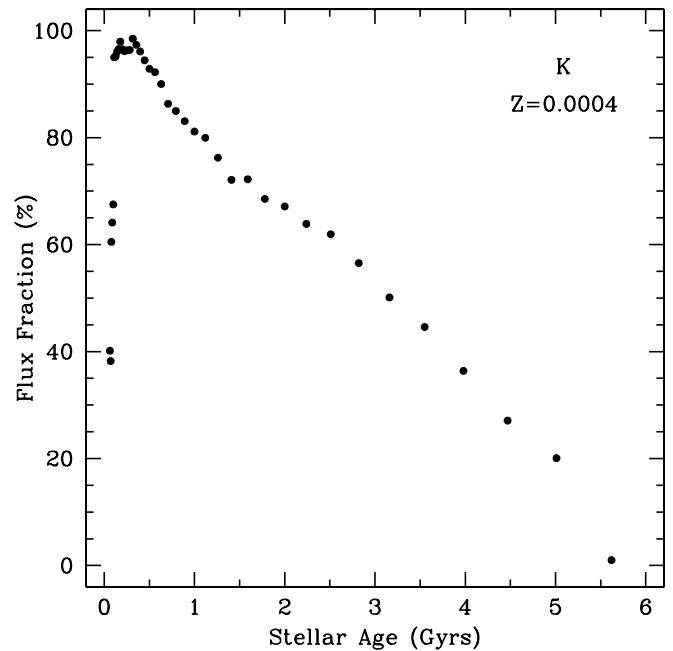


FIG. 10.—Fraction of the light of a burst of star formation contributed by stars brighter than $M_{K_s} = -7.5$ with respect to the total flux from all stars, as a function of the age. The plot is derived from isochrones generated using a Salpeter initial mass function and an isochrone with metallicity $Z = 0.0004 Z_{\odot}$.

were changed from 2.0 to 4.0 Mpc. We repeated the star detection process and recalculated the resolved/total ratio; it agreed with the first to within 0.2%. Also, from our entire sample we see no trend in the resolved/total ratio with distance. We conclude that over the range of distance sampled here, results for the flux ratios are not affected by variations in resolution.

The flux ratios for the resolved galaxies observed at CFHT are reported in Table 3 (in percentages). No ratios are given for the galaxies observed at OAN-SPM, as we did not quantify the resolved flux due to the lower spatial resolution. The resolved fluxes for all galaxies are very small in comparison with the total fluxes; in most cases the ratio is less than 5%. In fact, the true ratios are even lower given that the resolved population is contaminated to varying degrees by foreground stars. Ratios in J are 1.5–2 times larger than in K_s . Thus, the total NIR flux in a dI appears to be contributed mainly by stars with $M_{K_s} \gtrsim -7.5$, with K_s being less sensitive than J to the population of luminous stars.

One can employ population syntheses (Girardi et al. 2000, 2002) to evaluate the fraction of the flux from a burst of star formation contributed by stars brighter than $M_{K_s} = -7.5$. Although we do not know the detailed history of star formation in the dwarfs, we can look at how the proportion of stars brighter than $M_{K_s} = -7.5$ for any given burst depends on when the burst occurred, and thereby judge what our “old population” really represents. We performed this analysis using a Salpeter initial mass function, $N(M) = AM^{-2.35}$, and isochrones for metallicity $Z = 0.0004 Z_{\odot}$, which is typical for a low-metallicity dI. Figure 10 plots the flux fraction as a function of stellar age. The peak of the distribution is around 0.2–0.3 Gyr, with almost all the flux in a burst contributed by stars brighter than $M_{K_s} = -7.5$ mag. The proportion is above 50% for bursts younger than about 3 Gyr. For bursts older than about 6 Gyr, there are no stars brighter than $M_{K_s} = -7.5$ mag. Since 3 Gyr is a very generous definition of “recent” star formation, it is clear that the resolved fluxes represent the majority of the flux from such stellar populations. Given that the resolved flux is also a small fraction of the total flux, the

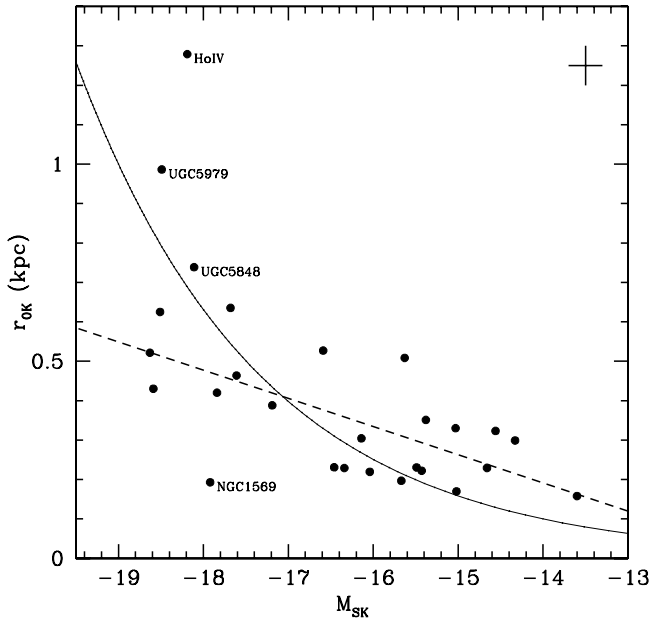


FIG. 11.—Correlation between the scale length and the absolute sech magnitude in K_s . The three labeled galaxies at top left are expected to have larger errors, while NGC 1569 is known to be a starburst. The dotted line represents a least-squares fit to the rest of the points, whose coefficients are given in eq. (15). The solid curve shows a locus of constant central surface brightness, specifically, $\mu_{0K} = -19 \text{ mag arcsec}^{-2}$.

remaining flux is a reliable measure of the flux from the underlying galaxy, unperturbed by recent star formation.

The appropriate age to associate with the unresolved component depends on how much the light of this component is contaminated by unresolved stars that have formed alongside the resolved component. A constraint can be gained from the fraction of light that is resolved. Suppose all resolved stars came from a single burst. Define $R_b(t)$ to be the flux from resolved burst stars, i.e., those brighter than $M_K = -7.5 \text{ mag}$, and $U_b(t)$ to be the flux from unresolved burst stars, i.e., stars fainter than $M_K = -7.5 \text{ mag}$, both at time t since the burst. Then the fraction of burst stars resolved at time t is $k(t) = R_b(t)/[R_b(t) + U_b(t)]$. Approximate the light of all stars formed prior to the burst to be unresolved and call the flux U_{old} . Then the fraction of the total light of all stars ever formed that are observed to be brighter than $M_K = -7.5 \text{ mag}$ is $f = R_b(t)/[R_b(t) + U_b(t) + U_{\text{old}}]$. It can be shown that

$$k(t) = \frac{f + f U_{\text{old}}/U_b}{1 + f U_{\text{old}}/U_b}. \quad (14)$$

Given a constraint on U_b/U_{old} and an observation of f , it is possible to solve for k . With the aid of Figure 10, the age t of the burst can be estimated. If we require that less than 10% of the old component be burst stars, then the observation that $f = 0.05$ requires the burst to have happened in the last 4 Gyr. Even though the actual star formation history may be more complicated, this analysis constrains the age of the unresolved component in dIs to be greater than 4 Gyr.

8.2. Correlations

Here we examine correlations between different properties of the dIs listed in Table 3. To express sizes, we employ the semimajor axis r_{22} for K_s , r_{23} for J , and scale length r_0 for K_s . For the absolute magnitudes we use mostly the sech magnitude M_S and for comparison the isophotal magnitude M_I and the total magnitude M_T . To characterize the centers we employ the central

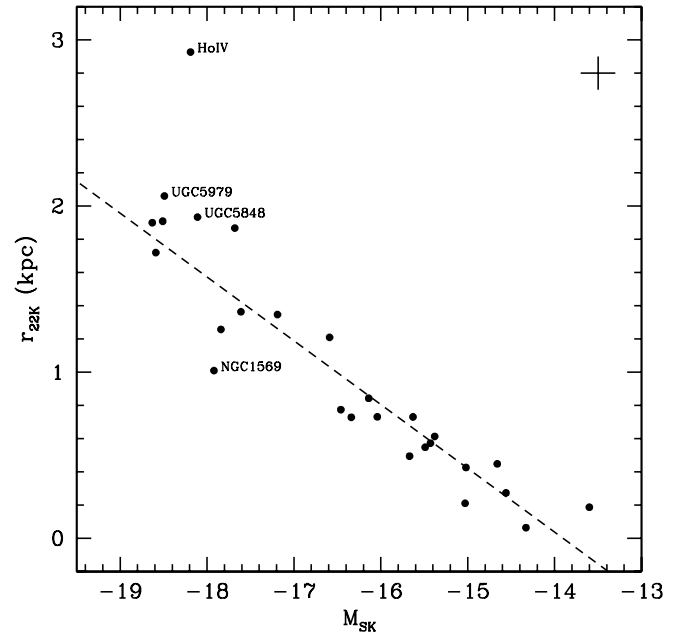


FIG. 12.—Correlation between the semimajor radius r_{22} and the absolute sech magnitude in K_s . The three labeled galaxies at top left are expected to have larger errors, while NGC 1569 is known to host a starburst. The dotted line represents a least-squares fit to the rest of the points, whose coefficients are given in eq. (16).

surface brightness μ_0 . To characterize motions we use W_{20} , the width of the $H\text{ I}$ line profile measured in km s^{-1} at 20% of the peak (included in Table 2). We focus on the K_s band, because it quantifies better the old population, but similar results are obtained in J . In each graph to be discussed below, the typical uncertainties in each parameter are plotted as an error cross.

8.2.1. Size and Brightness

The size of a dI is expected to correlate with the luminosity of the old component, which is responsible for most of the baryonic mass. A linear trend between the logarithm of the radius and the absolute magnitude was seen previously in the B band by Hidalgo-Gamez & Olofsson (1998), who studied a sample including 176 irregular galaxies (spiral/irregular and irregular). Comparing BCDs with dIs, Papaderos et al. (1996) found a clear linear trend of the scale length as a function of the absolute magnitude in B , with BCDs showing a steeper correlation than dIs. In the NIR a similar correlation has been found between the effective radius and luminosity in H , based on a larger sample of different types of galaxies, but the scatter is pretty large (Scodreggio et al. 2002).

Figures 11 and 12 show, respectively, the relation between the scale length r_0 and the semimajor axis r_{22} (both in kpc), as a function of the sech magnitude M_S . Both plots show good correlations; of the 27 galaxies having data in our sample, only four points appear to reside outside the linear trends: UGC 5979, UGC 5848 (our most distant targets, both having uncertain distances), Ho IV (one of our largest targets), and NGC 1569 (well known for its starburst). Rejecting the four deviant points, a linear fit in K_s gives the following solutions:

$$r_0 = (-0.81 \pm 0.24) + (-0.07 \pm 0.01)M_S, \quad (15)$$

$$r_{22} = (-5.34 \pm 0.40) + (-0.38 \pm 0.02)M_S. \quad (16)$$

We mention here that the correlation between the semimajor radius and the sech magnitude is not artificial (see eq. [11]), as we found a very similar trend replacing the sech with the total

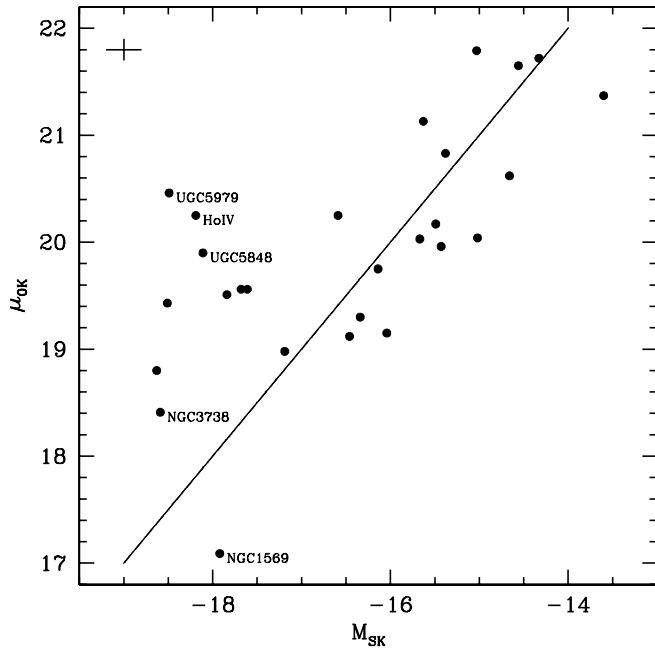


FIG. 13.—Correlation between the central surface brightness μ_0 and the absolute sech magnitude in K_s . The three labeled galaxies at left are expected to have larger errors, while NGC 1569 is known to have a central starburst. The solid line shows a locus of constant scale length, specifically, $r_{0K} = 0.4$ kpc.

magnitude. Based on equation (10), the absolute magnitude is expected to be a linear combination of the central surface brightness and the logarithm of the scale length, i.e.,

$$M_S = k + \mu_{0S} - 5 \log r_0, \quad (17)$$

where k is a constant. The thin curve in Figure 11 represents a curve of constant surface brightness, $\mu_{0K} = -19$ mag arcsec $^{-2}$. Clearly, the dwarf sequence is one of varying central surface brightness.

The uncertainties in r_0 , r_{22} , and r_{23} are determined mostly by the errors in the galaxy distances, because formal fitting errors are small (about 2%). The TRGB (employed in 20 cases) gives an error of about 10%. The brightest blue stars (used in nine cases) yield a scatter as large as 50% in distance. Hubble distances (employed in only two cases, UGC 5848 and UGC 5979) are supposed to be good to about 12%, although over the distance range covered here, local flow corrections are significant.

The correlations confirm that brighter dIs are larger. The fact that r_0 grows with luminosity also reveals that bright dIs have a larger central plateau. Correlations with the sech magnitudes are tighter than with isophotal and total magnitudes, in the latter case confirming the closer connection to the underlying mass.

8.2.2. Central Surface Brightness

In B , Hidalgo-Gomez & Olofsson (1998) did not find any correlation between the surface brightness and the absolute magnitude based on a sample of 176 irregular galaxies. Using a larger sample, observed also in B , Papaderos et al. (1996) studied the central surface brightness of the underlying exponential component as a function of the total luminosity. Notwithstanding the large scatter, there was a suggestion that the central surface brightness grows with increasing luminosity for dwarf galaxies other than BCDs.

Figure 13 shows the central brightness μ_0 as a function of the sech magnitude M_S . Rejecting the four outliers discussed above, there is a clear trend between the two parameters, in the sense that more luminous galaxies have brighter cores. Probably this has not

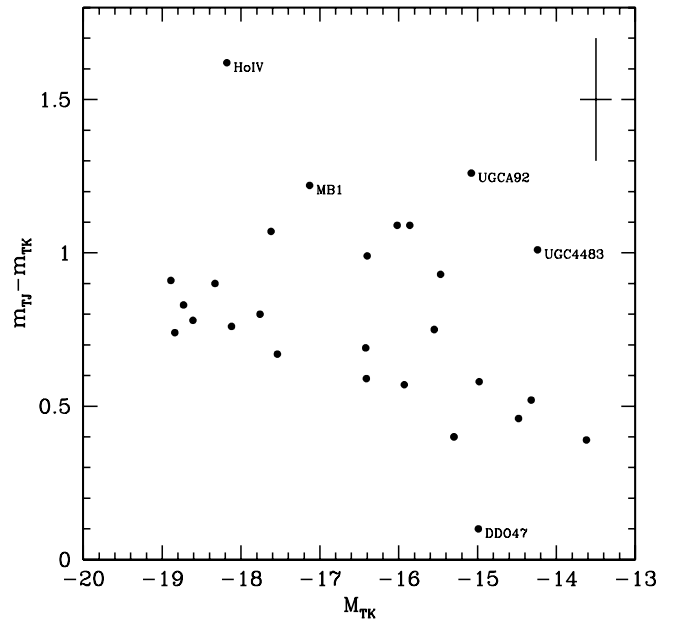


FIG. 14.—Correlation between the total color and the absolute total magnitude in K_s . UGC 4483, UGCA 92, and DDO 47 are very faint, Ho IV is larger than the FOV, and MB 1 suffers high reddening.

previously been seen so clearly because of the failure to separate young and old components. Moreover, rejecting NGC 3738 (which also hosts a burst), the correlation appears to level off at high luminosities, suggesting an upper limit to the central density of mass.

From equation (17) the absolute magnitude is expected to depend linearly on the central surface brightness. The solid line in Figure 13 represents the line of constant scale length, $r_{0K} = 0.4$ kpc.

A plot of the central surface brightness versus the resolved/total ratios does not show any correlation. This suggests that the fraction of the light that is young is not directly linked to the density in the core.

No correlation has been found between the central surface brightness and the scale length. This shows that both variables are required to define the SBP and luminosity.

8.2.3. Colors

In the B band, Hidalgo-Gomez & Olofsson (1998) found no relation between their colors and absolute magnitudes for a subsample including 89 irregular galaxies. Employing a larger less homogenous dwarf sample, Scodreggio et al. (2002) also did not find a correlation between $B - H$ colors and the logarithm of H luminosity, although for spirals a linear trend is visible.

As Figure 14 shows, our data reveal a correlation between colors and total magnitudes, with brighter galaxies being redder. Similar trends are obtained using the isophotal and sech magnitudes. Only a few points stand outside the trend, including UGCA 92, UGC 4483, and DDO 47 (all very faint), Ho IV (larger than the field), and MB 1 (suffering high reddening). The cause of the variation with magnitude is unlikely to be the star formation rate because the central surface brightness and color do not depend on the fraction of light that is resolved. Also, across any given dwarf, the color does not vary much with radius (see § 7.6). Rather, the reddening is more likely to be a manifestation of increasing metallicity. Following previous research in the visible (e.g., Richer & McCall 1995), the metallicity is expected to correlate with the NIR luminosity, with brighter galaxies having higher metallicities. The colors in Figure 14

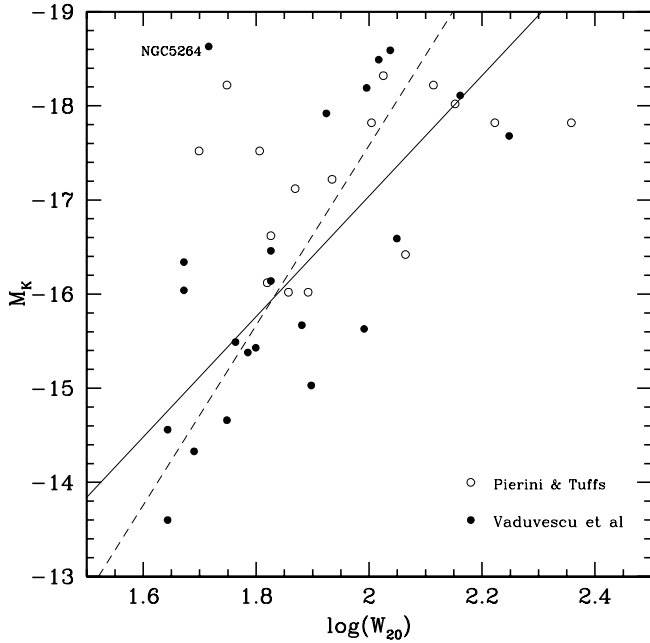


FIG. 15.— M_K as a function of the logarithm of the neutral hydrogen line width, W_{20} (km s^{-1}). Sech magnitudes are plotted for our field dIs (filled circles), while total magnitudes are plotted for the Virgo dwarfs examined by Pierini & Tuffs (1999) (open circles).

imply that the light is entirely dominated by evolved stars (Girardi et al. 2000, 2002). Galaz et al. (2002) showed that the $J - K_s$ color index is clearly very metal sensitive and relatively age insensitive. Assuming a single stellar metallicity, the $J - K_s$ colors can vary by at most 0.15 mag as a result of differing star formation histories. This is about 3 times less than the color range we see in Figure 14. On the other hand, a variation by a factor of 15 in metallicity is expected to lead to about 0.3 mag variation in color, which is much closer to the range observed.

8.2.4. The Tully-Fisher Relation

For luminous disk galaxies, the absolute magnitudes correlate with H I line width, i.e., rotational velocities (Tully & Fisher 1977). However, it is not clear how well dIs, known to rotate slowly, follow the Tully-Fisher correlation, because it is unknown how random motions scale with mass and how much star formation perturbs luminosities.

In a study of 50 giant and dwarf galaxies selected from the Virgo Cluster Catalogue, Pierini & Tuffs (1999) presented evidence that luminous dIs follow the Tully-Fisher relation in K' , but their sample only went as faint as $M_K = -17$. Of our field dI sample, 22 galaxies have W_{20} measurements listed in the Third Reference Catalog of Bright Galaxies (RC3; de Vaucouleurs et al. 1991).⁹ Figure 15 plots with filled circles their sech absolute magnitudes versus $\log W_{20}$. On the same diagram, 16 dwarfs from Pierini & Tuffs (1999) are plotted with open circles. The absolute magnitudes were calculated from the apparent K' magnitudes taken from the quoted paper using an updated Virgo distance modulus of 30.62 mag anchored to the maser distance to NGC 4258 (Freedman et al. 2001; see the Appendix). For these galaxies, too, we employed W_{20} from the RC3.

As one can see from Figure 15, M_K correlates with W_{20} down to $M_K = -13.5$, albeit with a standard deviation of 0.98 mag and

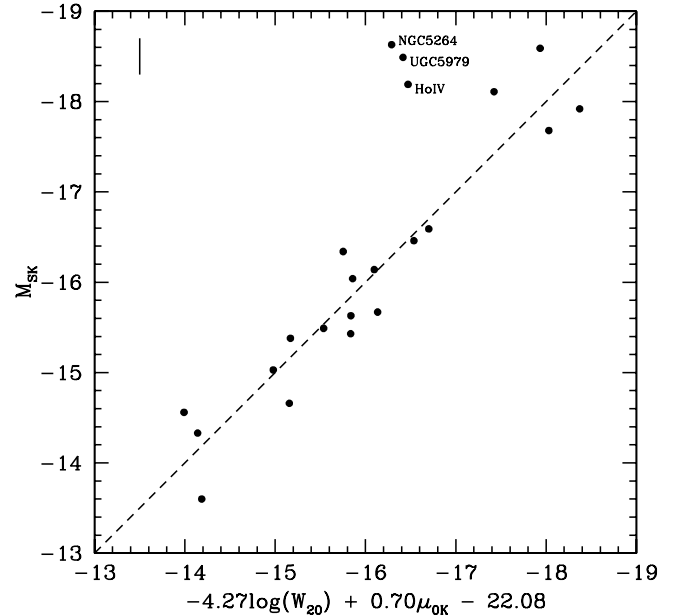


FIG. 16.—Sech magnitude in K_s vs. the logarithm of the neutral hydrogen line width, W_{20} (km s^{-1}), and the central surface brightness, μ_0 . Note the reduced scatter compared with the Tully-Fisher relation shown in Fig. 15. The error bar at the upper left of the diagram shows the typical error in M_K arising from the uncertainty in the TRGB distance. The photometry for Ho IV and the distances for UGC 5979 and NGC 5264 are questionable.

a correlation coefficient of only 0.57. The most deviant point in our sample is NGC 5264, possibly because of an uncertain distance based on its radial velocity. A linear fit to our galaxies, excluding NGC 5264, gives a slope of -6.4 ± 1.3 . The fit is shown as a solid line in Figure 15. Our data overlap the faint end of the NIR diagram of Pierini & Tuffs (1999). Fitting spirals and dwarfs together, these authors found a slope of -9.7 ± 0.3 . The dashed line in Figure 15 shows their slope. Although the error quoted by Pierini & Tuffs (1999) suggests a more solid fit than ours, their fit is biased toward spirals. Their points for dwarfs look more scattered than ours. Both sets of data show a larger spread at the bright end, possibly because of enhanced rotational motions and the varying angles at which they are viewed. However, little change is observed when W_{20} is corrected for tilt on the basis of isophotal axis ratios.

8.2.5. A Fundamental Plane for dIs

The large scatter in the Tully-Fisher relation hinted that dI luminosities depend on more than just internal motions. Thus, we investigated whether residuals might be linked to the central surface brightness μ_0 or the scale length r_0 .

Figure 16 shows that the absolute sech magnitude is strongly correlated with the linear combination of $\log W_{20}$ and the central surface brightness, μ_0 . The three deviant points are UGC 5979 (whose distance is approximate, determined from the Hubble law), Ho IV (a galaxy larger than the FOV, also having an approximate distance determined using the three brightest blue stars), and NGC 5264 (which might be classified as a “dwarf spiral” [e.g., Lee et al. 2003a], in which case tilt corrections to W_{20} should be applied). Rejecting these three outliers, the fit can be expressed through the following correlation:

$$M_S = (-4.27 \pm 0.61) \log(W_{20}) + (0.70 \pm 0.09)\mu_0 - (22.08 \pm 2.40). \quad (18)$$

⁹ Accessed with VizieR, online at CDS; <http://vizier.u-strasbg.fr/viz-bin/VizieR>.

With an rms deviation of 0.43 mag and a correlation coefficient of 0.91, we think this may provide a useful avenue for determining distances to dIs.

We compared W_{20} with W_{50} (Karachentsev et al. 2004) and found that W_{20} produced a stronger correlation. We also tried correcting for inclination, computing $W_{20}/(2 \sin i)$ using the algorithm of Staveley-Smith et al. (1992) along with the ellipticities listed in Table 2. However, the improvement was very small, suggesting that internal motions in the majority of our dwarfs are predominantly random. This is a major advantage over spirals in the sense that good distances can be determined without correcting W_{20} for tilt.

Denoting the mean surface brightness by $\langle SB \rangle$, equation (18) implies that $L_K \propto \sigma^{1.71} \langle SB \rangle^{0.70}$, where L_K is the total luminosity and σ is the central velocity dispersion. For elliptical galaxies, Djorgovski & Davis (1987) found $L \propto \sigma^{3.45} \langle SB \rangle^{-0.86}$ in the Gunn r band. Dwarf irregular galaxies are distinct from elliptical galaxies in that luminosity increases with surface brightness.

9. CONCLUSIONS

Nearby dwarf irregular galaxies (dIs) and blue compact dwarfs (BCDs) are important probes for studying the formation and evolution of galaxies. In an effort to extract information about old stellar populations, a sample of 34 dIs in the field, most of them located closer than 5 Mpc and having known or soon-to-be-known metallicities, have been imaged using NIR arrays at the CFHT in Hawaii and the OAN-SPM in Mexico, between 2001 and 2004. Besides detecting the unresolved component in 25 of 34 targets, which is primarily associated with the old stellar population, we also resolved stars as faint as $M_{K_s} = -7.5$ mag out to 5 Mpc.

By separating the resolved sources associated with each galaxy from the unresolved component, we were able to determine for the first time the contribution from the resolved stellar component to the total light in the NIR. In nearly all galaxies, the resolved population brighter than $M_{K_s} = -7.5$ mag represents less than 5% of the flux in K_s and 7%–10% in J . Population syntheses reveal that stars brighter than $M_{K_s} = -7.5$ contribute more than 50% of the light from bursts as far back as 3 Gyr. Given the small contribution of the resolved flux to the total flux of dIs, together with the constant NIR colors, one can regard NIR fluxes for dIs as approximating the light from a population older than about 4 Gyr and thereby use them as gauges of stellar mass.

SBPs of the unresolved components have been successfully fitted across the whole range of radii with a hyperbolic secant function defined by only two parameters: the central surface brightness μ_0 and the scale length r_0 . Only two cases (NGC 1569 and NGC 3738) showed flux excesses in the center, but both are known to host central starbursts similar to those seen in BCDs. These two galaxies will be addressed in a future paper devoted to BCDs (Vaduvescu et al. 2005). Isophotal, total, and sech NIR magnitudes have been calculated for all galaxies showing an unresolved component, along with semimajor axes at $\mu_J = 23$ mag arcsec $^{-2}$ and $\mu_{K_s} = 22$ mag arcsec $^{-2}$.

We searched for correlations between galaxy size, absolute magnitude (sech, isophotal, and total), central surface brightness, color, and the resolved/total ratio. Good linear correlations were found between the scale length and the sech magnitude and between the semimajor axis and the sech magnitude. Also, correlations were found between colors and isophotal magnitudes and between the central surface brightness and the sech magnitude. Overall, galaxies with more luminous old components are larger, redder, and brighter in the center. Thus, size, color, and the extent of the central plateau appear to be influenced by the mass of the old

component. Redder colors may be a consequence of increasing metallicity, because the fraction of the light that is young shows no trend with absolute magnitude or central surface brightness.

At the lower luminosity end of our dI sample, the Tully-Fisher relation shows considerable scatter in K_s . The scatter appears to be tied to variations in surface brightness. A new “fundamental plane” is found to relate the sech absolute magnitude, the central surface brightness, and the hydrogen line width uncorrected for tilt. The residuals are low enough (0.4 mag) that it offers considerable potential as a distance indicator for star-forming dwarfs.

For 29 galaxies, CMDs for the resolved component have been derived. Three CMDs include more than 1000 stars in both K_s and J , while another 15 CMDs have more than 100 stars. Most of the CMDs show a main blue finger centered around $J - K_s = 1$ mag. In some cases, a red tail extends from the finger out to $J - K_s = 2.5$ mag. The color profiles of the unresolved components show a remarkably constant $J - K_s = 0.8$ – 1.0 mag, which is close to the color of the main finger in the CMDs.

We thank the CFHT and OAN-SPM time allocation committees for granting us the opportunity to observe. CFHT is operated by the National Research Council of Canada, the Centre National de la Recherche Scientifique, and the University of Hawaii. Thanks are conveyed to the National Research Council of Canada for funding the observing expenses of O. V., M. L. M. is grateful to the Natural Sciences and Engineering Research Council of Canada for its continuing support. M. G. R. acknowledges financial support from CONACyT grants 37214-E and 43121 and DGAPA grant IN112103. M. G. R. thanks G. Garcia, G. Melgoza, F. Montalvo, and S. Monrroy for their help with the observations. For our data reductions, we used IRAF, distributed by the National Optical Astronomy Observatory, which is operated by the Association of Universities for Research in Astronomy, Inc., under cooperative agreement with the National Science Foundation. O. V. acknowledges Ivo Saviane for some interesting discussions related to similar work. Special thanks are also conveyed to the anonymous referee whose suggestions helped us to improve the paper.

APPENDIX A

The majority of the distances adopted in this paper have been derived using modern photometric data with either primary or secondary distance indicators. All distances have been homogenized to a common distance scale anchored by the maser distance to NGC 4258 (Herrnstein et al. 1999). Furthermore, the distance estimates have been homogenized to a common extinction scale. Specifically, all but one of the Galactic extinction estimates originate from the reddenings of Schlegel et al. (1998, hereafter SFD98). The reddening of MB 1 has been assumed to be identical to that of Maffei 1 (Fingerhut et al. 2003). The reddenings have been converted to broadband extinctions using the York Extinction Solver (YES).¹⁰ Given an SFD98 reddening for a target, YES computes the corresponding optical depth at $1 \mu\text{m}$ (τ_1) using an elliptical spectral energy distribution (SED; on which SFD98 reddenings are based), then converts this value into broadband extinctions in the desired filters. By employing

¹⁰ The York Extinction Solver is a Web-based application developed in the Department of Physics and Astronomy, York University, and hosted by the Canadian Astronomy Data Centre. It can be accessed at <http://cadwww.hia.nrc.ca/yes>.

YES to calculate broadband extinctions and using an SED representative of a target appropriately redshifted and extinguished, we avoid source-dependent shifts in the effective wavelengths of broadband filters. Further details can be found in McCall (2004).

The homogenized distance estimates are listed in Table 2 along with the distance method, original distance reference, and τ_1 . The homogenization process for each distance method is described briefly in the following paragraphs. Further details will be provided in a forthcoming paper by R. L. Fingerhut et al. (2005, in preparation).

A1. TIP OF THE RED GIANT BRANCH

Twenty dIs in our sample have distances determined from the absolute magnitude of the TRGB, which marks helium ignition in the degenerate core of low-mass stars. In the I band, the TRGB has been found to be nearly invariant over a wide range of metallicities (see, e.g., Lee et al. 1993), thereby serving as a powerful standard candle. We adopt the value of $M_{I,\text{TRGB}} = -4.06 \pm .07$ mag (Ferraresse et al. 2000), which is calibrated by galaxies with Cepheid distances anchored to an LMC distance of $\mu_{\text{LMC}} = 18.5 \pm 0.13$ mag. The NGC 4258 distance scale brings the LMC distance closer by 0.19 mag, inducing an increase in $M_{I,\text{TRGB}}$ by this same amount. The modification to $M_{I,\text{TRGB}}$ has no effect on the uncertainty in this quantity due to the equivalent error bars on the LMC distance in both systems. Furthermore, $M_{I,\text{TRGB}}$ was derived from I -band photometry corrected for Galactic extinction using SFD98 reddenings, but with a slightly larger value for $A_I/E(B - V)$ than the average of the values computed by YES for the galaxies used to calibrate the TRGB. However, at the low reddenings of the TRGB calibrators, the different values of $A_I/E(B - V)$ have a negligible effect on A_I . As a result, $M_{I,\text{TRGB}}$ does not need to be shifted to our extinction scale. We therefore adopt $M_{I,\text{TRGB}} = -3.87 \pm 0.07$ mag.

The apparent magnitudes of the TRGB for the dIs in our sample have been corrected for extinction using the Galactic extinction as a reasonable estimate of the total extinction. This has been justified by H. Lee et al. (2005, in preparation), who found that the total extinction of dIs as estimated from the Balmer decrement in H II regions is equivalent, within errors, to the Galactic extinction determined from independent methods.

The dominant sources of uncertainty in the TRGB distances are the uncertainty in $M_{I,\text{TRGB}}$ and the uncertainty in the apparent I -band magnitude of the TRGB. For the galaxies in our sample with TRGB distances, the average uncertainty in the latter quantity is 0.17 mag. Hence, the average error associated with the TRGB distance moduli is 0.18 mag.

A2. BRIGHTEST BLUE STARS

Nine galaxies have distances determined from the average B magnitude of the three brightest stars (3BS method). The most recent calibration of this method is that of Karachentsev & Tikhonov (1994) based on a sample of 43 galaxies. Improved distance estimates and Galactic extinctions are now available for a large part of this sample, so we have recalibrated the 3BS method using the 29 galaxies that now have either TRGB or Cepheid distances. After homogenizing the TRGB and Cepheid distances,

as well as the extinction estimates, to our adopted scale, we obtain a new 3BS calibration of

$$M_{B3} = -0.49(B_{3,0} - B_0^T) - 3.90, \quad (\text{A1})$$

where $B_{3,0}$ is the average magnitude of the three brightest stars in B corrected for extinction, M_{B3} is the absolute magnitude corresponding to $B_{3,0}$, and B_0^T is the total magnitude of the galaxy in B corrected for extinction. Equation (A1) has an rms scatter of 0.97 mag. Further details of this calibration will be provided in a future paper. As with the TRGB distances, the 3BS distances have been derived using the Galactic extinction as an estimate of the total extinction of dIs.

A3. SURFACE BRIGHTNESS FLUCTUATIONS

For UGC 4998, the only modern distance estimate is the value obtained by Jerjen et al. (2001) from the SBF method in the R band. Using TRGB distances for a sample of dE galaxies, they construct a semiempirical calibration for the SBF method as a function of $B - R$ color. Jerjen et al. (2001) judge the uncertainty in distances derived from their calibration to be $\sim 10\%$. Because the zero point of the calibration is set by their adopted TRGB of $M_{I,\text{TRGB}} = -4.05$ mag, we shift their calibration by an additive constant of 0.18 mag to anchor it to our adopted value of $M_{I,\text{TRGB}}$. The galaxies used to calibrate the relation were corrected for Galactic extinction using the reddenings of SFD98. The reddenings are too low to have led to an appreciable difference in broadband extinctions compared with those computed by YES. Hence, the SBF calibration is already anchored to our adopted extinction scale and, with the shift of 0.18 mag, is sufficient for yielding distances homogenized to the rest of our sample.

A4. HUBBLE DISTANCES

Hubble distances have been adopted for the two most distant galaxies owing to their lack of suitable photometry. The Hubble constant is 79.2 ± 9.9 km s $^{-1}$ Mpc $^{-1}$ based on the Cepheid calibration of Freedman et al. (2001) but reanchored to the maser distance of NGC 4258. The heliocentric radial velocities were corrected for the solar motion toward the Local Group centroid using the solar apex vector determined by Courteau & van den Bergh (1999). The velocities were then further corrected for their infall toward the Virgo Cluster and the Great Attractor using the linear multiattractor model formulated by Marinoni et al. (1998). The uncertainty in the radial velocities of both galaxies is less than 1%. The uncertainty in the Hubble distances is therefore equal to the 12% uncertainty in the Hubble constant.

A5. MEMBERSHIP DISTANCES

The galaxies Cas 1 and MB 1 lack suitable data for a photometric distance estimate. However, both galaxies are believed to be associated with the nearby IC 342/Maffei group of galaxies. Recently, the distance to this group was found to be 3.3 ± 0.2 Mpc, which is the weighted average distance of its three dominant members (Fingerhut 2002; Fingerhut et al. 2003). We assign this distance to Cas 1 and MB 1.

REFERENCES

- Aloisi, A., et al. 2001, *AJ*, 121, 1425
 Aparicio, A., & Gallart, C. 1995, *AJ*, 110, 2105
 Aparicio, A., Tikhonov, N., & Karachentsev, I. 2000, *AJ*, 119, 177
 Bahcall, J. N., & Soneira, R. M. 1980, *ApJS*, 44, 73
 Bergvall, N., Rönnback, J., Masegosa, J., & Östlin, G. 1999, *A&A*, 341, 697
 Borissova, J., Georgiev, L., Kurtev, R., Rosado, M., Ivanov, V. D., Richer, M., & Valdez-Gutiérrez, M. 2000a, *Rev. Mex. AA*, 36, 151
 Borissova, J., Georgiev, L., Rosado, M., Kurtev, R., Bullesos, A., & Valdez-Gutiérrez, M. 2000b, *A&A*, 363, 130
 Bressan, A., Chiosi, C., & Fagotto, F. 1994, *ApJS*, 94, 63

- Buta, R., & McCall, M. L. 1999, *ApJS*, 124, 33
- Cioni, M.-R. L., & Habing, H. J. 2003, *A&A*, 402, 133
- . 2005, *A&A*, 429, 837
- Courteau, S., & van den Bergh, S. 1999, *AJ*, 118, 337
- Cruz-González, I., et al. 1994, *Proc. SPIE*, 2198, 774
- de Vaucouleurs G., et al. 1991, *Third Reference Catalog of Bright Galaxies* (Springer: New York)
- Djorgovski, S., & Davis, M. 1987, *ApJ*, 313, 59
- Dohm-Palmer, R. C., et al. 1998, *AJ*, 116, 1227
- Dolphin, A. E., et al. 2001, *MNRAS*, 324, 249
- . 2003, *AJ*, 125, 1261
- Drozdosvsky, I. O., Schulte-Ladbeck, R. E., Hopp, U., Greggio, L., & Crone, M. M. 2002, *AJ*, 124, 811
- Ferraresse, L., et al. 2000, *ApJ*, 529, 745
- Fingerhut, R. L. 2002, M.S. thesis, York Univ.
- Fingerhut, R. L., McCall, M. L., De Robertis, M., Kingsburgh, R. L., Komljenovic, M., Lee, H., & Buta, R. J. 2003, *ApJ*, 587, 672
- Fioc, M., & Rocca-Volmerange, R. 1999, *A&A*, 351, 869
- Freedman, W. L., et al. 2001, *ApJ*, 553, 47
- Galaz, G., Dalcanton, J. J., Infante, L., & Tresiter, E. 2002, *AJ*, 124, 1360
- Gavazzi, G., Franzetti, P., Scodreggio, M., Boselli, A., & Pierini, D. 2000, *A&A*, 361, 863
- Gavazzi, G., Zibetti, S., Boselli, A., Franzetti, P., Scodreggio, M., & Martocchi, S. 2001, *A&A*, 372, 29
- Girardi, L., Bertelli, G., Bressan, A., Chiosi, C., Groenewegen, M. A. T., Marigo, P., Salasnich, B., & Weiss, A. 2002, *A&A*, 391, 195
- Girardi, L., Bressan, A., Bertelli, G., & Chiosi, C. 2000, *A&AS*, 141, 371
- Grebel, E. K. 2001, *Ap&SS Suppl.*, 277, 231
- Greggio, L., Tosi, M., Clampin, M., de Marchi, G., Leitherer, C., Nota, A., & Sirianni, M. 1998, *ApJ*, 504, 725
- Guarnieri, M. D., Dixon, R. I., & Longmore, A. J. 1991, *PASP*, 103, 675
- Herrnstein, J. R., et al. 1999, *Nature*, 400, 539
- Hidalgo-Gamez, A. M., & Olofsson, K. 1998, *A&A*, 334, 45
- Huchtmeier, W. K., & Skillman, E. D. 1998, *A&AS*, 127, 269
- Hunter, D. A., Gallagher, J. S., & Rautenkranz, D. 1980, *BAAS*, 12, 838
- James, P. A. 1991, *MNRAS*, 250, 544
- . 1994, *MNRAS*, 269, 176
- Jerjen, H., Rekola, R., Takalo, L., Coleman, M., & Valtonen, M. 2001, *A&A*, 380, 90
- Karachentsev, I. D., Drozdovsky, I., Kajsins, S., Takalo, L. O., Heinamaki, P., & Valtonen, M. 1997, *A&AS*, 124, 559
- Karachentsev, I. D., Karachentseva, V. E., Huchtmeier, W. K., & Makarov, D. I. 2004, *AJ*, 127, 2031
- Karachentsev, I. D., Makarova, L. N., & Andersen, M. I. 1999, *MNRAS*, 307, L37
- Karachentsev, I. D., & Musella, I. 1996, *A&A*, 315, 348
- Karachentsev, I. D., & Tikhonov, N. A. 1994, *A&A*, 286, 718
- Karachentsev, I. D., et al. 2002a, *A&A*, 383, 125
- . 2002b, *A&A*, 385, 21
- . 2002c, *A&A*, 389, 812
- . 2003a, *A&A*, 398, 467
- . 2003b, *A&A*, 398, 479
- Kunth, D., & Östlin, G. 2000, *A&A Rev.*, 10, 1
- Lee, H., Grebel, E. K., & Hodge, P. W. 2003a, *A&A*, 401, 141
- Lee, H., McCall, M. L., Kingsburgh, R. L., Ross, R., & Stevenson, C. C. 2003b, *AJ*, 125, 146
- Lee, M. G., Freedman, W. L., & Madore, B. F. 1993, *ApJ*, 417, 553
- Makarova, L. 1999, *A&AS*, 139, 491
- Makarova, L., Karachentsev, I., Takalo, L. O., Heinaemaeki, P., & Valtonen, M. 1998, *A&AS*, 128, 459
- Makarova, L. N., & Karachentsev, I. D. 2003, *Astrophysics*, 46, 144
- Makarova, L. N., Karachentsev, I. D., & Georgiev, T. B. 1997, *Astron. Lett.*, 23, 378
- Manduca, A., & Bell, R. A. 1979, *PASP*, 91, 848
- Marigo, P., Girardi, L., & Chiosi, C. 2003, *A&A*, 403, 225
- Marinoni, C., Monaco, P., Guiricini, G., & Costantini, B. 1998, *ApJ*, 505, 484
- McCall, M. L. 2004, *AJ*, 128, 2144
- Méndez, B., Davis, M., Moustakas, J., Newman, J., Madore, B. F., & Freedman, W. L. 2002, *AJ*, 124, 213
- Nikolaev, S., & Weinberg M. D. 2000, *ApJ*, 542, 804
- Nikolaev, S., Weinberg, M. D., Skrutskie, M. F., Cutri, R. M., Wheelock, S. L., Gizis, J. E., & Howard, E. M. 2000, *AJ*, 120, 3340
- Papaderos, P., Loose, H.-H., Fricke, K. J., & Thuan, T. X. 1996, *A&A*, 314, 59
- Patterson, R. J., & Thuan, T. X. 1996, *ApJS*, 107, 103
- Persson, S. E., Murphy, D. C., Krzeminski, W., Roth, M., & Rieke, M. J. 1998, *AJ*, 116, 2475
- Pierini, D., & Tuffs, R. J. 1999, *A&A*, 343, 751
- Richer, M. G., & McCall, M. L. 1995, *ApJ*, 445, 642
- Schlegel, D. J., Finkbeiner, D. P., & Davis, M. 1998, *ApJ*, 500, 525 (SFD98)
- Schneider, S. E., Thuan, T. X., Mangum, J. G., & Miller, J. 1992, *ApJS*, 81, 5
- Scodreggio, M., Gavazzi, G., Franzetti, P., Boselli, A., Zibetti, S., & Pierini, D. 2002, *A&A*, 384, 812
- Sharina, M. E., Karachentsev, I. D., & Tikhonov, N. A. 1999, *Astron. Lett.*, 25, 322
- Skillman, E. D., Kennicutt, R. C., & Hodge, P. W. 1989, *ApJ*, 347, 875
- Staveley-Smith, L., Davies, R. D., & Kinman, T. D. 1992, *MNRAS*, 258, 334
- Stetson, P. B. 1987, *PASP*, 99, 191
- . 1992, in *ASP Conf. Proc. 25, Astronomical Data Analysis Software and Systems I*, ed. D. Worrall, C. Biemesderfer, & J. Barnes (San Francisco: ASP), 297
- Stetson, P. B., & Harris, W. E. 1988, *AJ*, 96, 909
- Tapia, M. 2003, *Rev. Mex. AA Conf. Ser.*, 19, 75
- Thuan, T. X. 1983, *ApJ*, 268, 667
- . 1985, *ApJ*, 299, 881
- Tikhonov, N. A., & Karachentsev, I. D. 1998, *A&AS*, 128, 325
- Tolstoy, E., et al. 1998, *AJ*, 116, 1244
- Tosi, M., Sabbi, E., Bellazzini, M., Aloisi, A., Greggio, L., Leitherer, C., & Montegriffo, P. 2001, *AJ*, 122, 1271
- Tully, R. B., & Fisher, J. R. 1977, *A&A*, 54, 661
- Vaduvescu, O., & McCall, M. 2004, *PASP*, 116, 640
- Vaduvescu, O., McCall, M. L., & Richer, M. 2005, *AJ*, submitted
- van der Kruit, P. C., & Searle, L. 1981, *A&A*, 95, 105
- Zwicky, F. 1965, *ApJ*, 142, 1293